A two-pronged approach to inhibit ferroptosis of MSCs caused by the iron overload in postmenopausal osteoporosis and promote osseointegration of titanium implant

Yulu Yang [a,1], Xianhui Zhang [a,1], Yao Yang [a], Pengfei Gao [a], Wuzhe Fan [a], Tao Zheng [a], Weihu Yang [a,*], Yu Tang [b,**], Kaiyong Cai [a,***]

[a] *Key Laboratory of Biorheological Science and Technology, Ministry of Education College of Bioengineering, Chongqing University, Chongqing, 400044, China*
[b] *Orthopedics Department, The Second Affiliated Hospital of Chongqing Medical University, Chongqing, 400010, China*

ARTICLE INFO

ABSTRACT

Postmenopausal osteoporosis (PMOP) is a prevalent condition among elderly women. After menopause, women exhibit decreased iron excretion, which is prone to osteoporosis. To design a specific titanium implant for PMOP, we first analyze miRNAs and DNA characteristics of postmenopausal patients with and without osteoporosis. The results indicate that iron overload disrupts iron homeostasis in the pathogenesis of PMOP. Further experiments confirm that iron overload can cause lipid peroxidation and ferroptosis of MSCs, thus breaking bone homeostasis. Based on the findings above, we have designed a novel Ti implant coated with nanospheres of caffeic acid (CA) and deferoxamine (DFO). CA can bind on the Ti surface through the two adjacent phenolic hydroxyls and polymerize into polycaffeic acid (PCA) dimer, as well as the PCA nanospheres with the repetitive 1,4-benzo-dioxan units. DFO was grafted with PCA through borate ester bonds. The experimental results showed that modified Ti can inhibit the ferroptosis of MSCs in the pathological environment of PMOP and promote osseointegration in two main ways. Firstly, DFO was released under high oxidative stress, chelating with excess iron and decreasing the labile iron pool in MSCs. Meanwhile, CA and DFO activated the KEAP1/NRF2/HMOX1 pathway in MSCs and reduced the level of intracellular lipid peroxidation. So, the ferroptosis of MSCs is inhibited by promoting the SLC7A11/GSH/GPX4 pathway. Furthermore, the remained CA coating on the Ti surface could reduce the extracellular oxidative stress and glutathione level. This study offers a novel inspiration for the specific design of Ti implants in the treatment of PMOP.

1. Introduction

Osteoporosis, an imperative global public health concern, particularly affects older women who have transitioned through menopause. Specially, postmenopausal osteoporosis (PMOP) is an increasingly prevalent condition [1,2]. For most postmenopausal women, osteoporotic fractures easily occur and sometimes need a permanent fixation system for treatment [3]. Titanium and titanium (Ti) alloys are commonly used in clinical fixation systems [4,5]. However, the decrease of bone mineral density in PMOP patients and the insufficient

osseointegration ability of Ti implants will lead to an aseptic loosening and implantation failure [6,7]. So, it's urgent to find a novel Ti implant decorated strategy for postmenopausal women from the pathogenesis of PMOP.

It's well known that postmenopausal women have a significant decrease in estrogen, leading to disorders of bone metabolism and the easy occurrence of PMOP [8]. However, except for the change in estrogen level, for PMOP patients, iron overload in the body is also a major clinical feature [9]. Iron is an essential trace element for many biological processes [10,11], but unbalanced iron metabolism enhances the risk of

---

certain bone problems, most notably osteoporosis [12,13]. After menopause, women have difficulty in discharging iron due to menstrual periods, resulting in iron overload in the body [14–17]. Although some studies have shown that iron overload induces bone loss and may be related to ferroptosis and oxidative stress [13]. these results were based on animal models and no real clinical cases to confirm it.

In this work, based on the plasma samples of postmenopausal patients with and without osteoporosis from the Gene Expression Omnibus (GEO) database, the differentially expressed miRNAs and DNAs were screened out. We found the main biological processes occurring in PMOP were signal transduction, cell growth, apoptosis, and cell communication. Some key genes (TP53, GPX4, MYC, KEAP, IL-6, JUN,

etc.) in PMOP pathogenesis mainly focused on ferroptosis, mitophagy, fatty acid biosynthesis, necroptosis, NOD-like receptor signaling pathway, adipocytokine signaling pathway, autophagy, etc. These results proved that in PMOP, excessive iron accumulation leads to the destruction of iron homeostasis [18,19]. Based on the important role of mesenchymal stem cells (MSCs) in the pathologic process of PMOP [20, 21]. we further explored the effect of excessive iron accumulation on MSCs. Excessive iron accumulation can cause oxidative stress and MSC cell death. Ferroptosis, a programmed cell death process, is characterized by lipid peroxidation, the accumulation of ROS, and iron overload [17,22]. Ferroptosis affects the occurrence and development of postmenopausal osteoporosis, regulating ferroptosis may be a novel
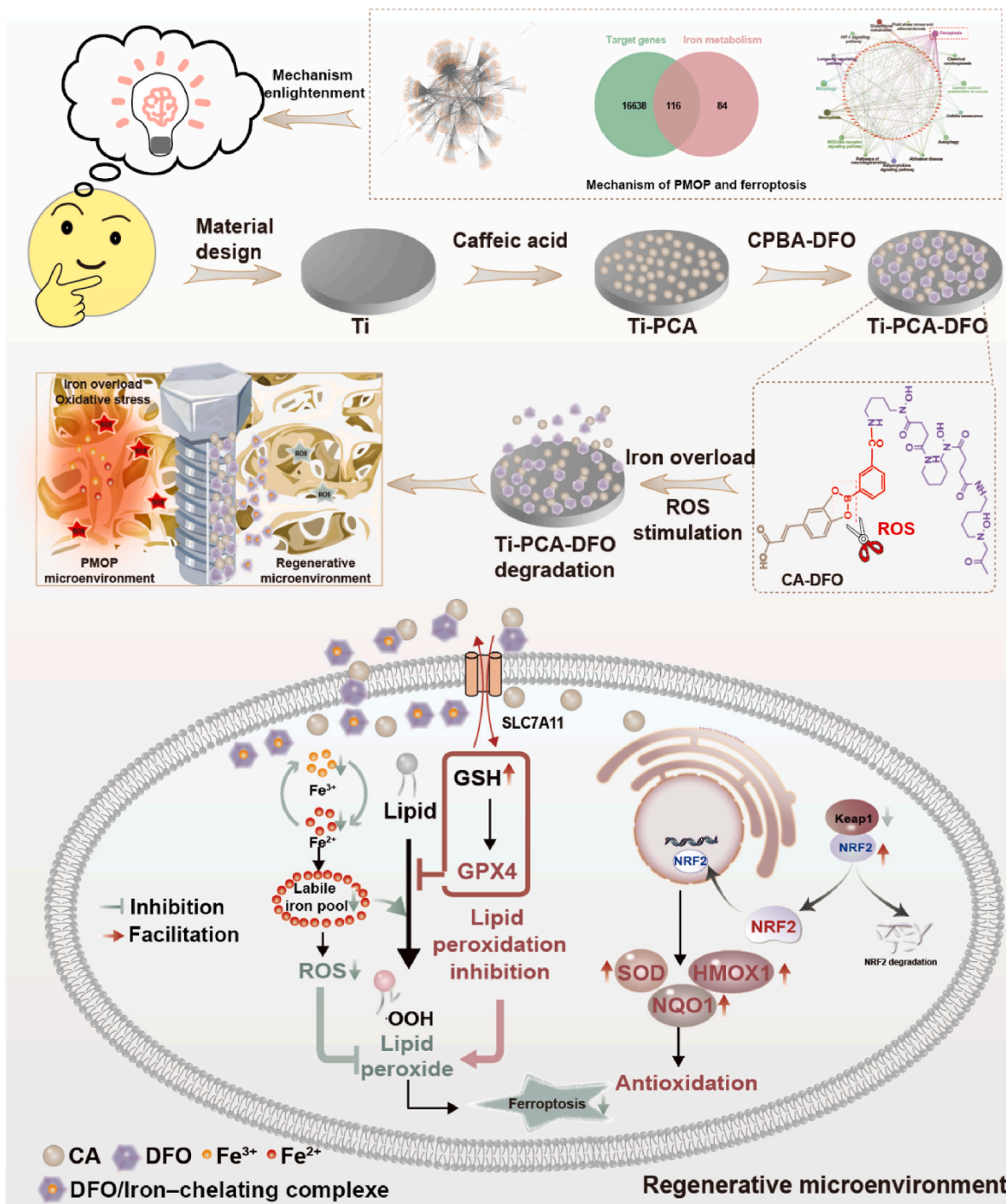
Scheme 1. The design and preparation of ROS-responsive CA-DFO coating modified Ti implant based on a comprehensive analysis of RNA-seq from plasma samples of postmenopausal osteoporosis patients, and schematic illustration of inhibiting ferroptosis of MSCs and promoting the osteointegration mechanism.

therapeutic strategy for postmenopausal osteoporosis [23–25]. Ti and Ti alloys are commonly used materials in clinical bone defect repair [26, 27]. However, oxidative stress and MSC cell death induced by excessive iron accumulation hindered bone integration in PMOP patients. Therefore, enhancing osseointegration through the reduction of oxidative stress and iron accumulation surrounding implants represents a potential strategy for optimizing implantation success in PMOP patients.

Based on the considerations above, deferoxamine (DFO) and caffeic acid (CA) were adopted in this work. DFO is an FDA-approved injectable drug for iron chelator, which can bind free iron and form iron complexes, and reduce intracellular iron absorption [28–30]. We constructed a responsive coating to realize the slow release of DFO in the high ROS microenvironment of osteoporosis. Caffeic acid is a polyphenolic compound whose structure (aromatic core, conjugated double bonds, and hydroxyl group) enables CA to both function as an antioxidant and to be highly chemically versatile and modifiable. Studies have shown that CA has self-polymerization and adhesion due to its special structure [31,32]. In addition, the two adjacent phenolic hydroxyl polyphenols of CA can bind on the surface of transition meal oxide liking TiO_2 by electron transfer, and polymerize into polycaffeic acid (PCA) by the auto-oxidation triggered radical chain-growth polymeriziont [33, 34]. In our previous work, we have investigated CA to repair ONFH [35]. We have found that oxidative stress is the main responsible for both ONFH and PMOP. In this work, we mainly investigate the feasibility of inhibiting ferroptosis under the condition of iron overload in PMOP by exploiting another important role of DFO, iron chelation.

To investigate a novel modifying Ti implant for PMOP, we initially investigated the pathogenesis of PMOP by transcriptome sequencing results from plasma samples of postmenopausal osteoporosis patients and obtained the main pathways and gene expression changes related to PMOP. Meanwhile, we have further verified the association between postmenopausal osteoporosis and ferroptosis of MSCs induced by excessive iron accumulation. The above results guided the subsequent design of titanium implants for PMOP. Considering the two main factors of ferroptosis, lipid peroxidation and iron overload. We designed a novel titanium coating with caffeic acid and deferoxamine, which can inhibit ferroptosis of MSCs by chelation of excess iron and reduction of lipid peroxidation (Scheme 1). Firstly, DFO was grafted with carboxyphenylboric acid to form a small molecule CPBA-DFO through an amide reaction. It can combine with the caffeic acid self-polymerizing nanospheres coating on the Ti surface through the borate ester bond. Under normal physiological conditions, DFO could promote angiogenesis and osteogenesis. However, under the pathological environment of high reactive oxygen species (ROS) in osteoporosis, DFO could achieve ROS-responsive release through the breakage of the borate ester bond, thereby complexing iron and reducing the iron concentration around the implant. Meanwhile, the remained caffeic acid coating could reduce the oxidative stress and lipid peroxidation levels around the implant. Through the analysis of transcriptome data related to osteoporosis in the GEO database, the pathologic characteristics and related mechanisms of osteoporosis were explored. On this basis, titanium implants that can regulate ferroptosis and promote bone integration are designed, which provides a new idea for the development and design of biofunctional titanium implants. The modified titanium implants have the potential to enhance bone formation by modulating iron metabolism to suppress ferroptosis of MSCs and activating antioxidant systems, thereby facilitating osseointegration between bone and implants under osteoporosis. Using disease databases to develop optimal biomaterials for specific pathologies and analyzing the underlying mechanisms of PMOP bone repair through transcriptome data was lacking in previous studies. This provides a framework for future smart biomaterials design.

2. Results

2.1. The molecular mechanism of PMOP and its relationship with iron metabolism

To discover the possible pathogenesis of postmenopausal osteoporosis, miRNA data from the GEO database (GEO Series: GSE201543) were downloaded. The differentially expressed miRNAs based on the plasma samples of postmenopausal patients with and without osteoporosis were investigated first. A total of 110 differentially expressed miRNAs ($|\log_2 FC|>2$, *P-value* <0.05) were screened out and their relationship was presented with a heat map in Fig. 1A. Contrasting with the control group, 85 up-regulated miRNAs and 25 down-regulated miRNAs were found in the plasma of PMOP patients. GO analysis of miRNAs was performed to find the Biological Process (BP), Cellular Component (CC), and Molecular Function (MF) of these differentially expressed miRNAs. The main biological processes occurring in the plasma (Fig. 1B) were signal transduction, cell growth and/or maintenance, and cell communication, whose respective ratios in the whole BP were 20 %, 18 %, and 18 %. The cell components are mainly concentrated in the nucleus and cytoplasm (Fig. 1C). Meanwhile, there are a large number of transcription factor activities and transcription regulator activity in molecular function (Fig. 1D). Further, enrichment analysis of these differentially expressed miRNAs was run to find the main reactome pathways. The results in Fig. 1E showed that most miRNAs were enriched to four reactome pathways, including signal transduction, immune system, metabolism, and metabolism of proteins.

To further discuss the key genes in PMOP, the corresponding target genes from these 110 differentially expressed miRNAs were analyzed on mirWALK, and a total of 16754 target gene data were obtained in Fig. 1F. After menopause, women are prone to iron accumulation. So, taking into consideration the iron overload and high ROS in clinical manifestations, we sought 116 intersection genes from the target gene set and iron metabolism gene set as shown in the Venn diagram in Fig. 1G. GO enrichment analysis of the 116 intersection genes (Fig. 1H) showed that the most biological process concentrated in response to oxidative stress, cellular iron ion homeostasis, iron ion homeostasis, cellular transition metal ion homeostasis, transition metal ion homeostasis, iron ion transport, which are closely related to ferroptosis. Meanwhile, in cellular component and molecular function, the autophagosome, mitochondrial outer membrane, fatty acid ligase activity, iron ion transmembrane transporter activity, and ferric iron binding also play core roles in PMOP.

KEGG enrichment analysis was adopted for the 116 genes. Fig. 1I showed that the key genes in PMOP pathogenesis mainly include TP53, ALB, ACTB, GPX4, HMOX1, MYC, IL-6, RELA, etc. These genes are closely related to ferroptosis, oxidative stress, and bone metabolism [36–42]. The possible pathways of these key genes mainly focus on ferroptosis, mitophagy, necroptosis, NOD-like receptor signaling pathway, adipocytokine signaling pathway, autophagy, etc. Disease-related analysis (Fig. 1J) showed that these 116 genes-related diseases concentrated in skeletal-musculoskeletal diseases, including skeletal diseases, musculoskeletal disorders, congenital malformations, congenital malformations of the musculoskeletal system, osteosclerosis, osteogenesis implasia, etc.

Protein-Protein Interaction Networks (PPI) and the Matthews Correlation Coefficient (MCC) algorithm were taken again to investigate the hub genes in these 116 mutual genes. From Fig. 1K and 18 key genes including TP53, ALB, ACTB, HMOX1, GPX4, MYC, KRAS, IL-6, etc. are strongly linked to cell apoptosis and ferroptosis. To prove the roles of these mutual genes in the occurrence of PMOP, we got the hub genes related to miRNAs by the corresponding relationship of DNA and miRNA in Fig. 1L. By calculating the Pearson correlation coefficient in Fig. 1M, we found the ferroptosis-related miRNAs, e. g. hsa-miR-200b-3p (R = 0.914) and hsa-miR-340-5p (R = 0.999), were closely positive related to the occurrence of PMOP. Interestingly, hsa-miR-300 has a negative
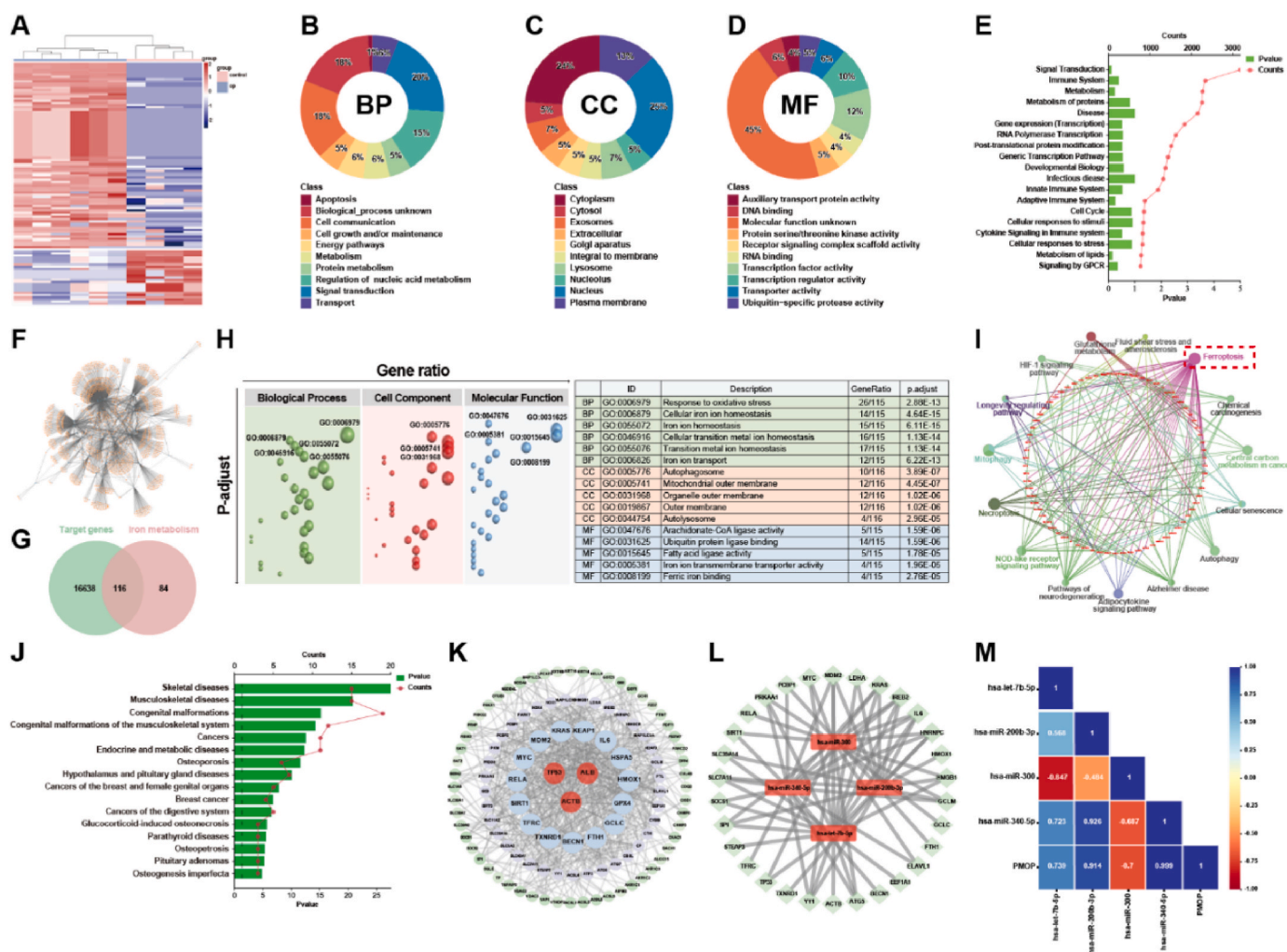
Fig. 1. (A) The differentially expressed miRNAs based on the plasma samples of postmenopausal patients with (Group B) and without (Group A) osteoporosis; (B) Biological processes, (C) Cellular component, and (D) Molecular function based on the differentially expressed miRNA; (E) The key reactome pathways of the differentially expressed miRNAs; (F) Graph of the corresponding target gene network of the differentially expressed miRNA; (G) The Venn diagram of target gene set and iron metabolism gene set; (H) GO enrichment results of the union 116 genes; (I) KEGG pathways of the union 116 genes; (J) Disease analysis of the union 116 genes; (K) Protein-protein interaction network and the hub genes of the union 116 genes; (L) The hub miRNAs and their correlation with the top 50 hub genes; (M) Pearson correlation coefficient between the hub miRNAs and the occurrence of PMOP. $|\log_2FC|>2$, *P-value* <0.05.

correlation with the occurrence of PMOP. The analysis of the public functional genomics data of PMOP proved that cell apoptosis, including ferroptosis, is the important pathogenesis of PMOP.

2.2. Iron accumulation and ferroptosis

Postmenopausal osteoporosis has a clinical symptom of iron accumulation [43]. Some studies have shown that excessive iron might negatively impact the balance of bone metabolism [44,45]. To further verify the relationship of osteoporosis, as well as ferroptosis, with iron overload, *in vitro* cytology experiments and transcriptome sequencing were adopted together. MSCs were cultured with different FAC solutions, and the cell viability (Fig. 2A) and osteogenic differentiation ability represented as alkaline phosphatase (ALP) (Fig. 2B) were detected. The results showed that the moderate Fe^{3+} (FAC, <100 μM) could promote cell growth and ALP activity. However, the excessive Fe^{3+} (FAC, ≥100 μM) would inhibit cell viability and ALP activity. Apoptosis, cell live/dead staining, mitochondrial membrane potential staining, GPX4 protein staining, and Calcein-AM staining were also performed to further verify the influences of iron overload on MSCs (Fig. 2C & D). In live/dead staining, the cell survival rate in the TCPS (tissue culture polystyrene) group was 99.5 %, but the ratio was 94.9 %

in the Fe group. Flow cytometry was taken to measure apoptosis levels of MSCs, and DFO was used as an inhibitor of ferroptosis. From Fig. 2C, contrasting with TCPS, the apoptosis levels in the other three groups increased diversely. Specifically, after co-culture with 100 μM Fe, no obvious difference was found in the early apoptosis of MSCs, and the late apoptosis of MSCs increased slightly. But when Fe is 200 μM, the early and the late apoptosis of MSCs, especially in the late apoptosis, enhanced obviously, and the total apoptosis of MSCs was 15.09 %. At the same Fe concentration, when DFO was added as the inhibitor of ferroptosis, the apoptosis of MSCs decreased significantly, and the total apoptosis of MSCs decreased from 15.09 % to 8.02 %, indicating the ratio of ferroptosis is about 7.07 %.

As the main symbols of ferroptosis, Calcein-AM, JC-1, and GPX4 immunofluorescence staining were performed. According to previous methods, Calcein-AM staining was used to indirectly characterize the changes in iron content in cells. From laser confocal microscopy (CLSM) in Fig. 2D & Figure S1, the fluorescence intensity of MSCs in the Fe group was weaker than that in TCPS. Because the fluorescence of Calcein-AM can be quenched by forming complexes with cytosolic iron, the weaker fluorescence intensity meant the higher intracellular iron ion content in the Fe group. Moreover, the JC-1 kit was used to detect mitochondrial membrane potential and apoptosis because excessive iron ions in MSCs
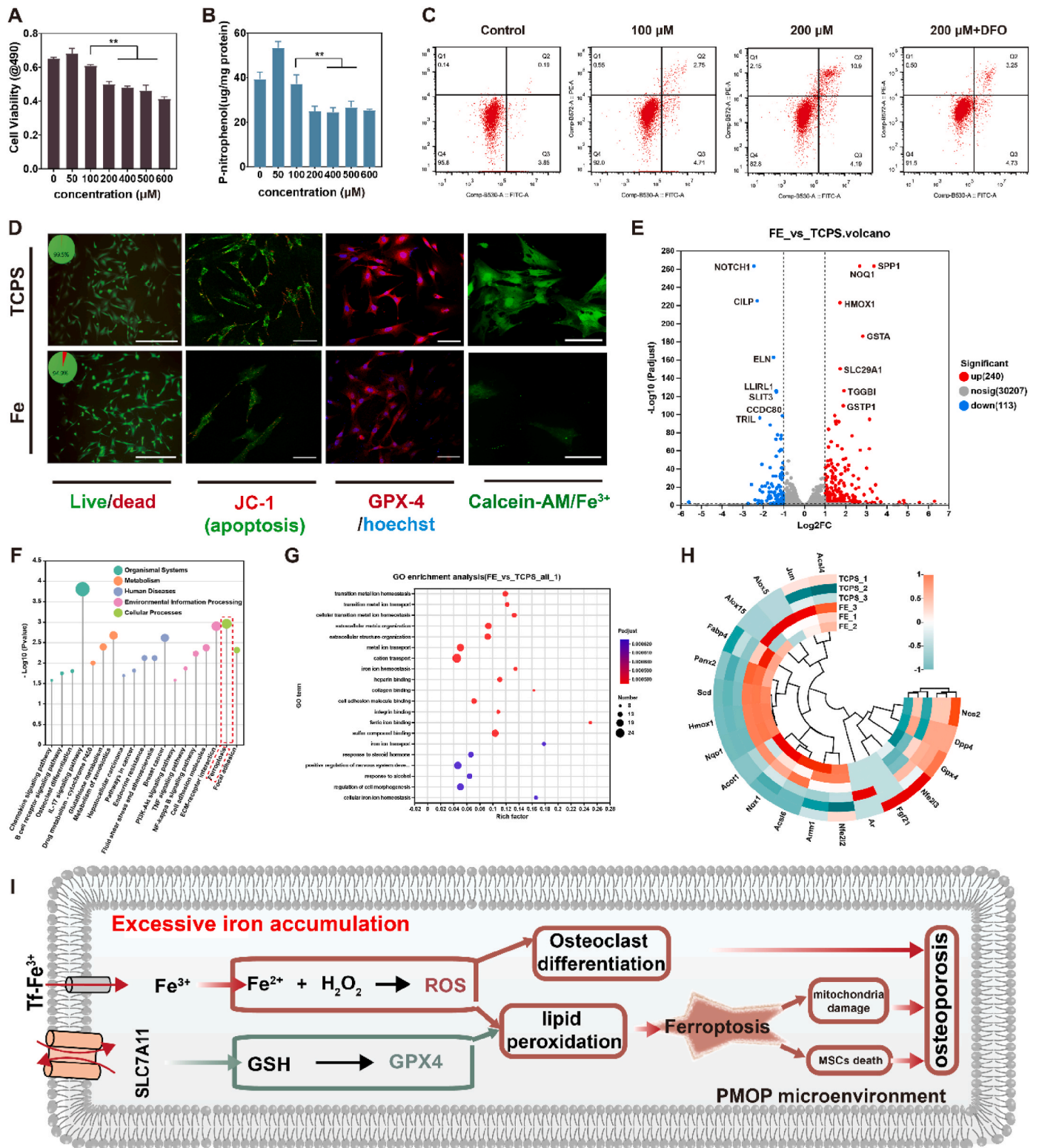
Fig. 2. (A) MSCs viability after treatment with different concentrations of Fe ions; (B) ALP content after treatment with different concentrations of Fe ions; (C) Flow cytometry detected the apoptosis levels of MSCs after varied treatments; (D) Live/dead staining of cells, CLSM observation of mitochondrial membrane potential changes; Immunofluorescence staining of GPX4, and Calcein-AM staining in the Fe and TCPS groups; (e) Volcano plot of differential genes in FE group compared with TCPS; (F) KEGG analysis of differentially expressed genes in FE group with TCPS group as control; (G) GO enrichment of differentially expressed genes in FE group compared to control TCPS; (H) Heatmap of the top 20 expressed genes related to ferroptosis; (I) Diagram of mechanism of ferroptosis induced by excessive iron. $|\log_2 FC|>2$, *P-value* <0.05. n = 3, **$p < 0.01$.

could cause changes in mitochondrial membrane potential. From the result of JC-1, the fluorescence of JC-1 in the Fe group decreased greatly, indicating the mitochondrial membrane potential of MSCs was changed significantly by excessive iron ions. Meanwhile, the cytoskeleton of MSCs in the Fe group has shrunk contrasting with TCPS. As the most important antagonist molecule in ferroptosis, down-regulation of GPX4 is one of the most important symbols of ferroptosis. GPX4 immunofluorescence staining showed that GPX4 in the Fe group was decreased, meaning the occurrence of ferroptosis. These above results proved that excessive iron could lead to MSCs ferroptosis.

To further explore the iron metabolism mechanism, genetic responses of MSCs in a medium with and without Fe were revealed by RNA sequencing. The volcano plot (Fig. 2E) showed a total of 30207 genes sequenced, in which 240 genes were up-regulated and 113 genes were down-regulated. The significantly up-regulated genes were SPP1, NQO1, HMOX1, GSTA1, SLC19A1, GSTP1, etc., which are the key genes related to oxidative stress and ferroptosis. The significantly down-regulated genes included NOTCH1, CILP, ELN, LL1RL1, SLIT3, CCDC80, TRIL, etc. KEGG enrichment analysis (Fig. 2F) was used to reveal gene functions. The main enrichment pathways in organic

system, metabolism, and cellular processes, were IL-17 and osteoclast differentiation pathways, glutathione metabolism, and ferroptosis pathway, respectively, in the FE group. The GO enrichment analysis (Fig. 2G) revealed that the differentially expressed genes (DEGs) were significantly enriched in intracellular and extracellular iron ion transport, iron ion homeostasis, and other related metal ion transport pathways, as well as *in vivo* metal ion homeostasis. The results of *in vitro* cell experiments and the genomic characteristics suggested that excess iron may activate oxidative stress, fatty acid metabolism, and ferroptosis pathways, which would lead to MSCs ferroptosis.

Based on the above results, we screened the top 20 genes related to ferroptosis, which were presented with a heatmap in Fig. 2H, and the possible mechanism map was drawn in Fig. 2I. A high concentration of Fe ions could increase the intracellular iron, thus inducing apoptosis and ferroptosis of MSCs. Cell viability and osteogenesis were significantly inhibited in the presence of iron overload. **Because** ACLS4 and ALOX15 activated polyunsaturated fatty acid oxidation, leading to the accumulation of lipid peroxides [46]. Meanwhile, the NRF2 pathway was activated and the expression of its downstream genes, HMOX1 and NQO1, were up-regulated. Moreover, the expression of GPX4 decreased. Based

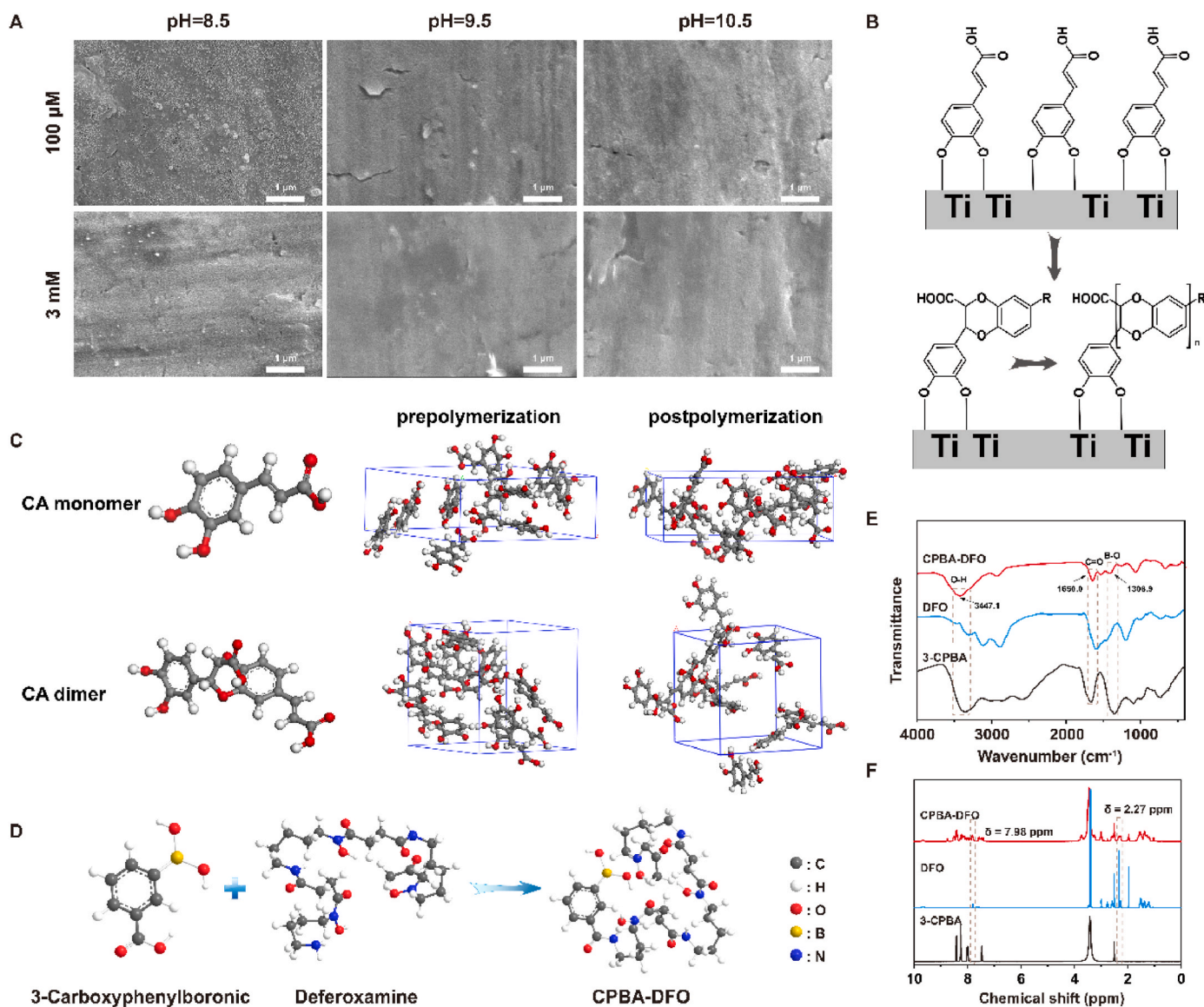**Fig. 3.** (A) SEM images of self-polymerized caffeic acid products on titanium surfaces at different pH and concentration; (B) Possible mechanism for the formation of self-polymerized caffeic acid particles on titanium surfaces; (C) MD simulation of caffeic acid monomer and dimer polymerization; (D) Synthesis process of CPBA-DFO; (E) Fourier transform infrared spectrum of CPBA-DFO; (F) ^{1}H NMR spectra of CPBA-DFO.

on the above pathways, iron overload will lead to oxidative stress and ferroptosis of MSCs, and decrease their osteogenic differentiation potential [47].

2.3. Preparation and characterization of Ti-PCA-DFO

Caffeic acid represents the o-diphenol structure of many plant-derived polyphenols, which has antibacterial, anti-inflammatory, anti-oxidant and other pharmacological activities. Caffeic acid undergoes auto-oxidation, especially in alkaline environments. Its monomers

initially form dissociated states and then oxidize O_2 in solution to form a superoxide radical. Subsequently, the monomer transforms into a carbon-oxygen radical or carbon-centered radical, which occurs by electron transfer. Some of the carbon-oxygen or carbon-centered radicals continue to transfer one electron and transform into the phenolic acid o-benzoquinone. Thus, we explored the auto-oxidation of caffeic acid on the titanium surface at various pH levels to create a functional coating with a specific topology. As shown in Fig. 3A, when immersed in a caffeic acid solution (100 μM, pH 8.5), a PCA film forms on the Ti surface, with approximately 50 nm microspheres evenly dispersed
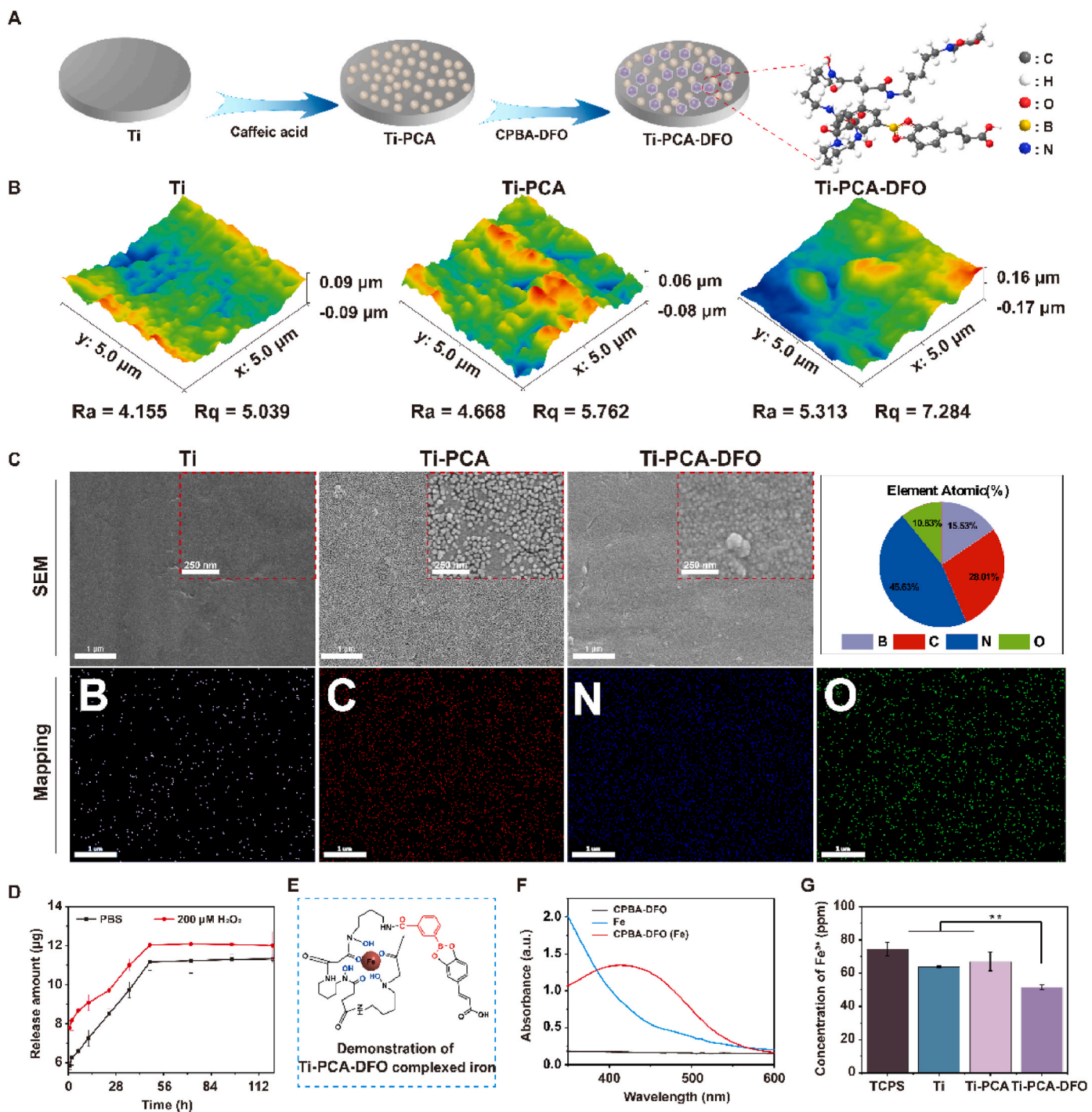
Fig. 4. (A) Synthesis diagram of titanium surface modification (Ti-PCA-DFO); (B) AFM images of Ti, Ti-PCA and Ti-PCA-DFO; (C) SEM images of Ti, Ti-PCA and Ti-PCA-DFO, and mapping images and atomic ratio of Ti-PCA-DFO; (D) Cumulative release curve of DFO from Ti-PCA-DFO surface; (E) Illustration of the iron complex in Ti-PCA-DFO; (F) UV spectra of Fe^{3+} complexed by CPBA-DFO; (G) ICP measurement of different groups after Fe^{3+} adsorption. n = 3, *$p < 0.05$, **$p < 0.01$.

throughout the membrane. During caffeic acid auto-oxidation, intermediates of single electron transfer may bond through C–C or C–O coupling to form dimers, as shown in Fig. 3B. The dimer still contains the o-diphenol hydroxyl group, which can be further oxidized to produce free radicals and polymerize. However, due to the high concentration of caffeic acid (3 mM) and the high pH (9.5 and 10.5), the caffeic acid will polymerize into a single piece, resulting in uniform surface morphology. Molecular dynamics (MD) simulation was used to analyze the changes in the polymerization of caffeic acid monomers and dimers on a titanium surface, to explore the molecular mechanism of caffeic acid auto-polymerization. Fig. 3C shows that CA monomers easily aggregate to form a continuous structure, while CA dimers tend to form discontinuous aggregates. Based on this, CA dimers may form uniform nanospheres on the surface of titanium through intermolecular cyclization reactions such as Michael addition, Diels-Alder reaction, and π-π packing. At high concentrations (3 mM) and high pH levels (9.5 and 10.5), CA may form a PCA film through rapid polymerization of the monomer. However, under mild conditions, CA tends to form dimers and nanospheres on the Ti surface.

Deferoxamine (DFO) is an FDA-approved iron chelator, which can bind free iron and be applied to treat chronic iron overload. To achieve high ROS-responsive release DFO, in this work, we first synthesized a CPBA-DFO compound via an amide reaction (Fig. 3D). FTIR and ^{1}H NMR (Fig. 3E & F) results showed that CPBA-DFO was synthesized successfully. In detail, in the FTIR spectrum of DFO, a double peak around 3300 cm^{-1} was a characteristic peak of the amino group in DFO, which disappeared in CPBA-DFO due to the amide reaction. Meanwhile, a new peak in CPBA-DFO at 1650 cm^{-1} was attributed to the C=O stretching vibration of the amide reaction (Fig. 3E). In the ^{1}H NMR spectra (Fig. 3F), a peak at $\delta = 2.27$ ppm is the characteristic absorption peak of the hydrogen atom of NH$_2$ in DFO. After the amide reaction, the $\delta = 2.27$ ppm peak disappeared, and the characteristic peak of hydrogen atoms in the amide bond $\delta = 7.98$–8.10 ppm was widened. The results of FTIR and ^{1}H NMR proved that DFO was successfully grafted on CPBA via amide reaction.

To improve the ability of implant integration with surrounding bone in PMOP patients, we designed a novel implant that can alleviate oxidative stress and iron accumulation around the bone (Fig. 4A). The CPBA-DFO compound could be grafted onto PCA film via the dynamic borate ester bonds, and the sample was named Ti-PCA-DFO. So, after coating with CPBA-DFO, the microsphere structure on the Ti-PCA surface became indistinctly because of the shield of CPBA-DFO and the surface roughness also increased (Fig. 4B & C). EDS spectra results showed that element B appeared on the Ti-PCA-DFO surface, and the content of B element was 15.52 %. The content of the N element was 45.56 %. In addition, the chemical composition of the different surfaces was analyzed by XPS (Figure S2), and the Ti surface has the characteristic elemental peaks of C(1s), O(1s), and Ti(2p). After CPBA-DFO formed a bidentate complex with caffeic acid on Ti-PCA-DFO, the characteristic elemental peaks of B and N could be found on the Ti-PCA-DFO surface. The contact angle results of Ti, Ti-PCA, and Ti-PCA-DFO showed that the caffeic acid coating reduced the contact angle, and the introduction of DFO had no obvious effect (Figure S3). AFM, FE-SEM, and XPS results proved that phenylboric acid-modified DFO was successfully grafted on the caffeic acid coating surface.

The ROS-responsive release of DFO was measured also. As shown in Fig. 4D, DFO could be released quickly in hydrogen peroxide solution because the borate ester bond in Ti-PCA-DFO could be broken in a high reactive oxygen environment. Specifically, in 200 μM H$_2$O$_2$ solution, the release of DFO was 9.10 μg at the first 12 h, while it was 6.54 μg in PBS. As for the cumulative release, after 96 h, the cumulative release amount of DFO in H$_2$O$_2$ was significantly higher than in PBS. To evaluate the iron ion chelated ability of different Ti samples, illustrated in Fig. 4E, the content of iron ions in different solutions was tested with ICP. Because DFO and Fe can form a complex, leading to an absorption peak at 430 nm in the UV spectrum. In Fig. 4F, the peak at 430 nm appeared in

CPBA-DFO, meaning CPBA-DFO still has the iron ion chelated ability. ICP results (Fig. 4G) showed that Ti-PCA-DFO could significantly reduce the content of iron in solution.

2.4. Assessment of cytoactive and osteogenesis

CCK-8 assay was used firstly to evaluate the biocompatibility for each group. Under normal conditions, no significant difference in cell viability was found between the Ti-PCA-DFO and Ti groups after 4 and 7 days (Fig. 5A). But for the Ti-PCA group, cell viability after 7 days was decreased slightly because the application of CA to normal cells may cause oxidative stress disorder in cells, resulting in a decrease of cell viability. To simulate the high ROS and iron-overloaded microenvironment in PMOP, a conditioned culture was performed by mixing normal low-glucose medium with 100 μM FAC and 100 μM H$_2$O$_2$. Under the iron overload condition, the cell viability in Ti-PCA-DFO was significantly higher than that of other groups after 4 days and 7 days (Fig. 5B). Meanwhile, to further evaluate the cytotoxicity of every sample, the cell live/dead staining was adopted. From Fig. 5C, although some dead cells were found in all groups, the cell mortality in Ti-PCA-DFO was significantly decreased to 3 %, contrasting with Ti (16 %) and Ti-PCA (9 %).

Fe^{3+} and ROS may affect cell membranes and cell morphology. In the staining observation of MSCs cytoskeleton (Fig. 5D), the cell morphology was varied in different groups. MSCs on the surface of Ti-PCA and Ti-PCA-DFO spread wider and better, but MSCs on the Ti surface shrunk obviously. The transcriptome of MSCs in conditioned culture was sequenced and analyzed accordingly. When compared with the Ti group, there were 1239 DEGs in Ti-PCA-DFO (Figure S4). KEGG and GO analysis (Figure S5 & S6) showed that these DEGs were mainly enriched in the pathways related to cell proliferation, such as cell cycle, immune response, DNA replication, apoptosis, and so on. A flow cytometer was constructed to detect the apoptosis level of MSCs on Ti, Ti-PCA, and Ti-PCA-DFO in a medium containing 100 μM FAC and 100 μM H$_2$O$_2$. The ratio of apoptotic cells to necrotic cells is an important index to study the level of apoptosis. As shown in Fig. 5E, Ti, Ti-PCA, and Ti-PCA-DFO groups induced 25.58 %, 19.84 %, and 12.26 % apoptosis, respectively. Therefore, Ti-PCA-DFO could significantly improve the viability of MSCs and reduce cell apoptosis under iron-overloaded microenvironment and oxidative stress in vitro. To observe the distribution of MSCs on Ti, Ti-PCA, and Ti-PCA-DFO at different periods under stressful conditions, we labeled DNA with PI. The DNA content was analyzed by flow cytometry and the proportions of G0/G1, S, and G2/M were calculated (Fig. 5F). After treatment with Ti, Ti-PCA, and Ti-PCA-DFO, the proportion of cells in the G0/G1 phase was 66.67 %, 68.84 %, and 62.78 %, respectively, indicating that MSCs on Ti, Ti-PCA may be blocked in the G0/G1 phase under iron overload microenvironment and oxidative stress. The S phase of MSCs on Ti-PCA-DFO was significantly increased, which indicated that Ti-PCA-DFO was beneficial to alleviating the obstruction of cell division and increasing cell proliferation in the environment of high iron and ROS. Based on the above results, contrasting with the Ti group, at the normal conditions, Ti-PCA-DFO had no toxic effect on MSCs. However, in the adverse environment of high iron and ROS, Ti-PCA-DFO exhibits a remarkable capacity to enhance the viability of MSCs. This novel bone implant material effectively supported MSCs survival under stressful conditions, mitigated cell death rates, and facilitated cellular proliferation.

To evaluate the in vitro osteogenic effect of Ti, Ti-PCA, and Ti-PCA-DFO, ALP, collagen secretion, and mineralization were qualitatively and quantitatively analyzed. ALP staining photos (Fig. 5G) showed that more ALP was generated on Ti-PCA-DFO after 7 days, and the quantitative result (Fig. 5H) showed that ALP activity of the Ti-PCA-DFO group was significantly higher than Ti. Moreover, as the marker of early and middle-stage osteogenesis, the secreted collagen after 14 days was stained and quantitatively detected. The results proved that MSCs on the Ti-PCA-DFO surface could secret the most collagen (Fig. 5I). Finally, the marker of mid to late osteogenesis, and mineralization level was
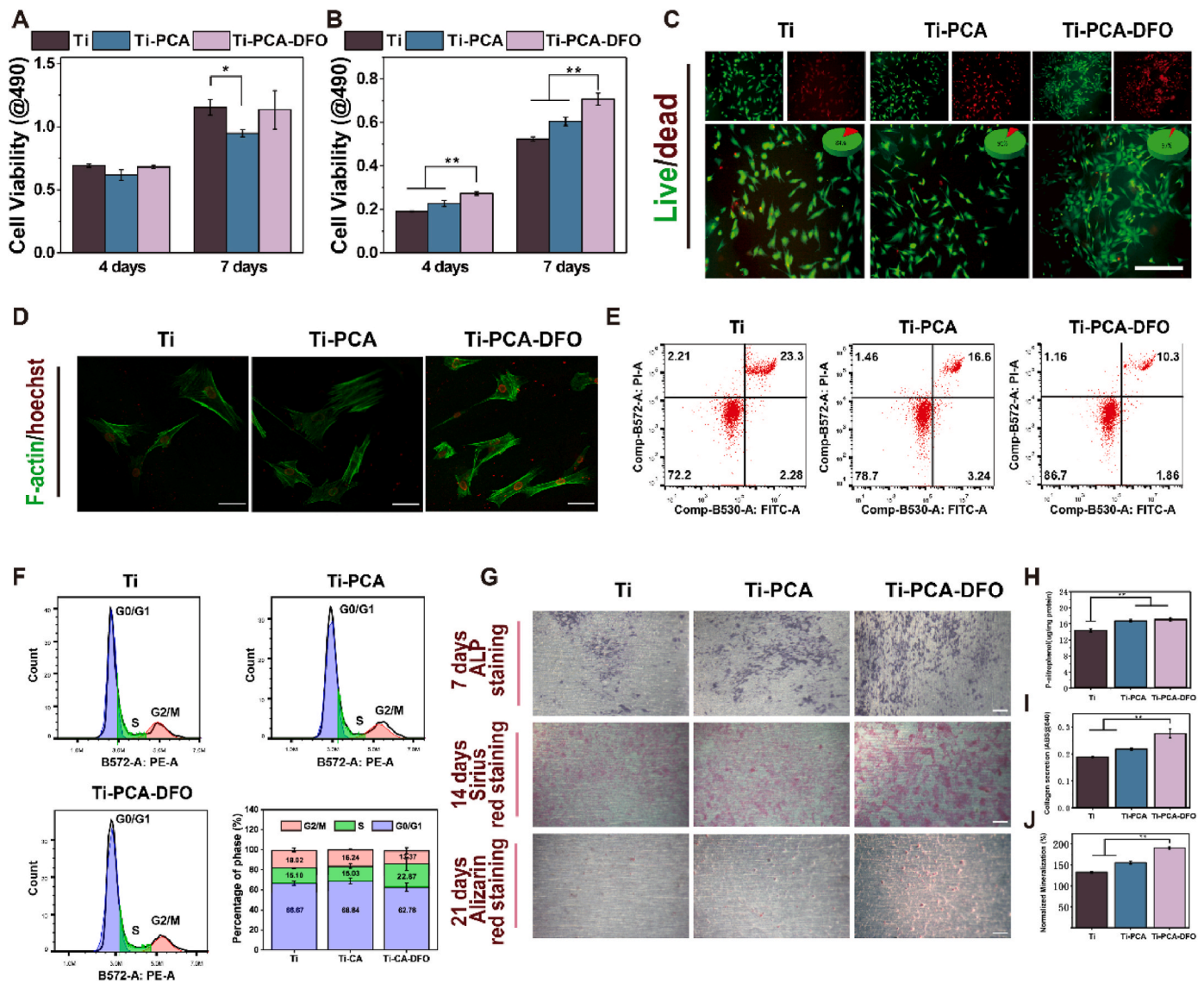
Fig. 5. MSCs viability after co-culturing with different samples in (A) normal medium and (B) conditioned medium; (C) Cell lived/dead staining on Ti, Ti-PCA, and Ti-PCA-DFO was observed in medium containing 100 μM FAC and 100 μM H_2O_2 after 48 h, Scale bar: 200 μm; (D) Cytoskeleton in each group after 48 h in the conditioned medium; Scale bar: 50 μm; (E) Flow cytometer detected the apoptosis levels of MSCs on Ti, Ti-PCA, and Ti-PCA-DFO in medium containing 100 μM FAC and 100 μM H_2O_2; (F) Cell cycle distribution of MSCs in different phases on Ti, Ti-PCA, and Ti-PCA-DFO in medium containing 100 μM FAC and 100 μM H_2O_2; (G) ALP staining, Sirius red staining, and Alizarin red staining of MSCs, Scale bar: 200 μm; (H) ALP quantitative, (I) Collagen quantitative, and (J) Mineralization quantitative analysis of MSCs. n = 4, *$p < 0.05$, **$p < 0.01$.

evaluated with the alizarin red staining and qualitative assay, the same tendency with collagen was found also (Fig. 5J). The *in vitro* osteogenic results showed that Ti-PCA-DFO has the best capability for osteogenesis, and the Ti-PCA group took the second place under stressful conditions.

2.5. Evaluation of the antioxidant activity and lipid peroxidation

The accumulation of iron-dependent lipid ROS plays a crucial role in all pathways leading to ferroptosis [46]. Lipid metabolism exhibits a close association with the occurrence of iron-mediated ferroptosis [48]. To assess the capacity for regulating oxidative stress and lipid metabolism, we examined lipid ROS levels, superoxide dismutase (SOD) activity, and malonaldehyde (MDA) in MSCs after co-culturing with Ti, Ti-PCA, and Ti-PCA-DFO in a medium containing 100 μM FAC and 100 μM H_2O_2. Lipid ROS indicates the destruction of membrane lipid peroxidation in response to ferroptosis. Firstly, lipid ROS was detected by C11 BODIPY 581/591. In Fig. 6A, Ti-PCA-DFO showed the lowest probe fluorescence intensity meaning less lipid ROS production in MSCs

on the Ti-PCA-DFO surface. Meanwhile, SOD activity was significantly increased in Ti-PCA-DFO (Fig. 6B). Furthermore, as one of the important products of membrane lipid peroxidation, MDA content (Fig. 6C) in Ti-PCA-DFO decreased significantly, meaning the reduction of lipid peroxidation in MSCs. The above results proved that Ti-PCA and Ti-PCA-DFO have good inhibition for lipid peroxidation and ROS due to the excellent antioxidant capacity of caffeic acid.

RNA sequencing was applied again. As shown in Fig. 6D, after coating with polycaffeic acid, a total of 1964 differentially expressed genes (DGs) were sequenced out, in which 955 genes were up-regulated and 1009 genes were down-regulated. These DGs could be clustered into 7 main clusters (Fig. 6E), in which the proportion of Cluster G is 83.99 % and the accumulated percent of associated genes was 335.19 %. The most important genes in Cluster G included AKT1, AKT3, PIK3CA, NFE2L2, NQO1, etc. Who were closely related to oxidative stress and antioxidant activity. Moreover, in Cluster F, GCLC, GPX3, GSS, and GSTA1 were the core genes, and they participated in the antioxidant pathway of glutathione metabolism. Furthermore, as the peroxidase
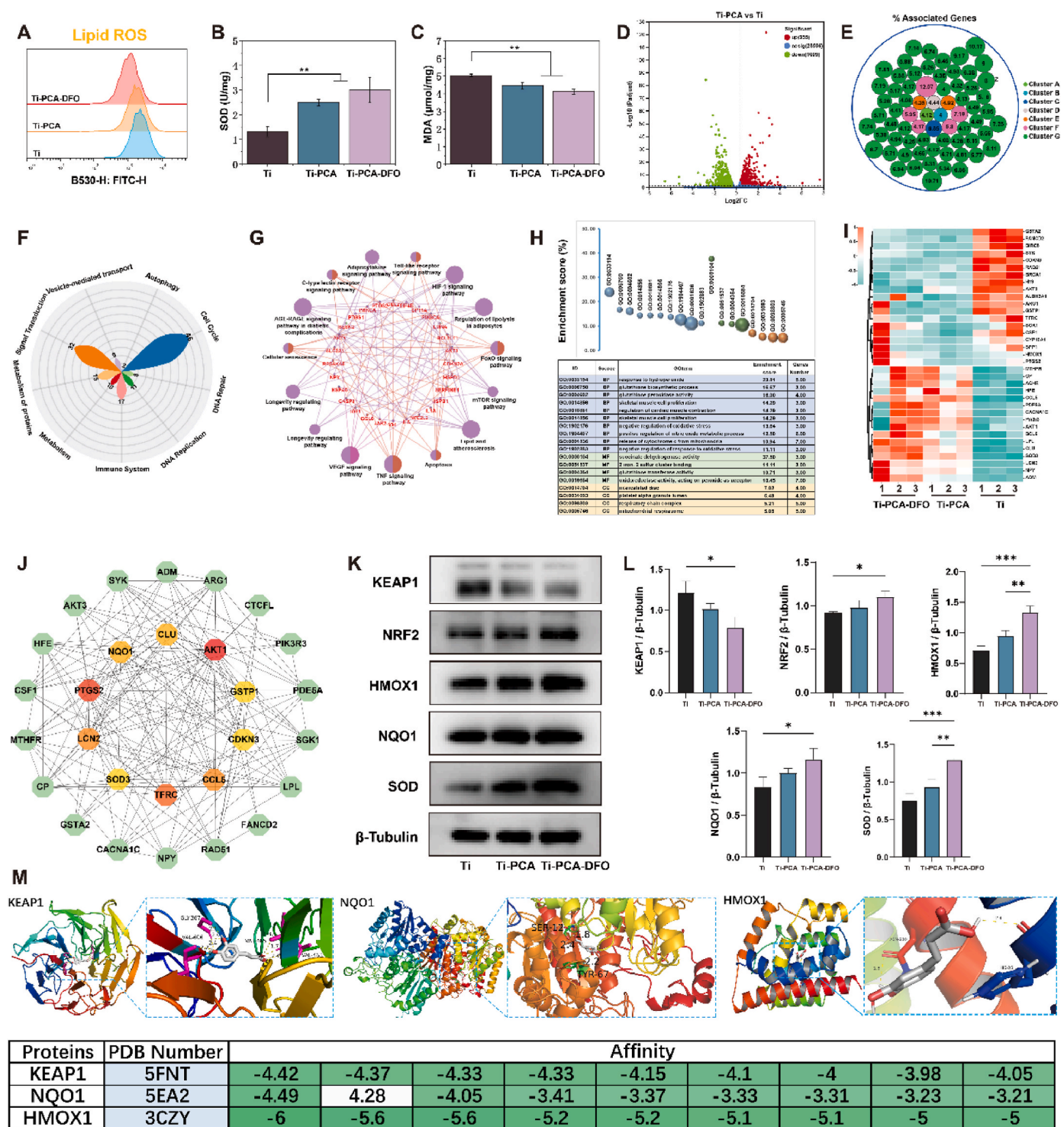
Fig. 6. (A) FCM analysis of lipid ROS content of MSCs on Ti, Ti-PCA, and Ti-PCA-DFO in a medium containing 100 μM FAC and 100 μM H_2O_2; (B) The SOD activity of MSCs on Ti, Ti-PCA, and Ti-PCA-DFO under conditioned culture; (C) The MDA content of MSCs on Ti, Ti-PCA, and Ti-PCA-DFO under conditioned culture; (D) Volcano plot of differential genes in Ti-PCA group compared with Ti group; (E) Cluster analysis of differentially expressed genes; (F) The main reactome pathways of differentially expressed genes; (G) KEGG and (H) GO enrichment analysis of DGs; (I) Heatmap of the DGS related to ferroptosis; (J) PPI network analysis of DGs and the core genes; Representative western blotting images (K) and quantitative analysis (L) of KEAP1, NRF2, HMOX1, NQO1, SOD; (M) The molecular docking of the core genes (KEAP1, NQO1, HMOX1) and caffeic acid. $n = 3$, *$p < 0.05$, **$p < 0.01$, ***$p < 0.001$.

synthase, PTGS1 and PTGS2 were the key genes in Cluster E, which were also closely related to lipid peroxidation. The reactome pathway (Fig. 6F) results showed that these DGs mainly enriched in 10 pathways, including cell cycle, signal transduction, immune system, metabolism, metabolism of proteins, etc. Some research has proved that the metabolism of *in vivo* lipid peroxide could influence oxidative stress. KEGG enrichment analysis was applied again, and the KEGG results (Fig. 6G) showed that the main pathways included the HIF-1 signaling pathway, regulation of lipolysis in adipocytes, FoxO signaling pathway, mTOR signaling pathway, lipid and atherosclerosis, and so on. These

pathways were closely related to oxidative stress and lipid peroxide. GO enrichment analysis results (Fig. 6H) showed that the most biological process in these DGs mainly focused on response to hydroperoxide, glutathione biosynthetic process, glutathione peroxidase activity, regulation of oxidative stress, and so on. Based on the above results, we picked genes associated with oxidative stress from these DGs, and their

expression was illustrated with a heatmap in (Fig. 6I). To find the key genes, PPI analysis was adopted, by calculating the number of nodes between different proteins, the hub genes, AKT1, CCL5, LCN2, SOD3, and NQO1, were picked out (Fig. 6J). Among them, SOD and NQO1 have attracted our attention. SOD is an antioxidant enzyme that can clear ROS and RNS in the body. NQO1 prevents oxidative damage to DNA under
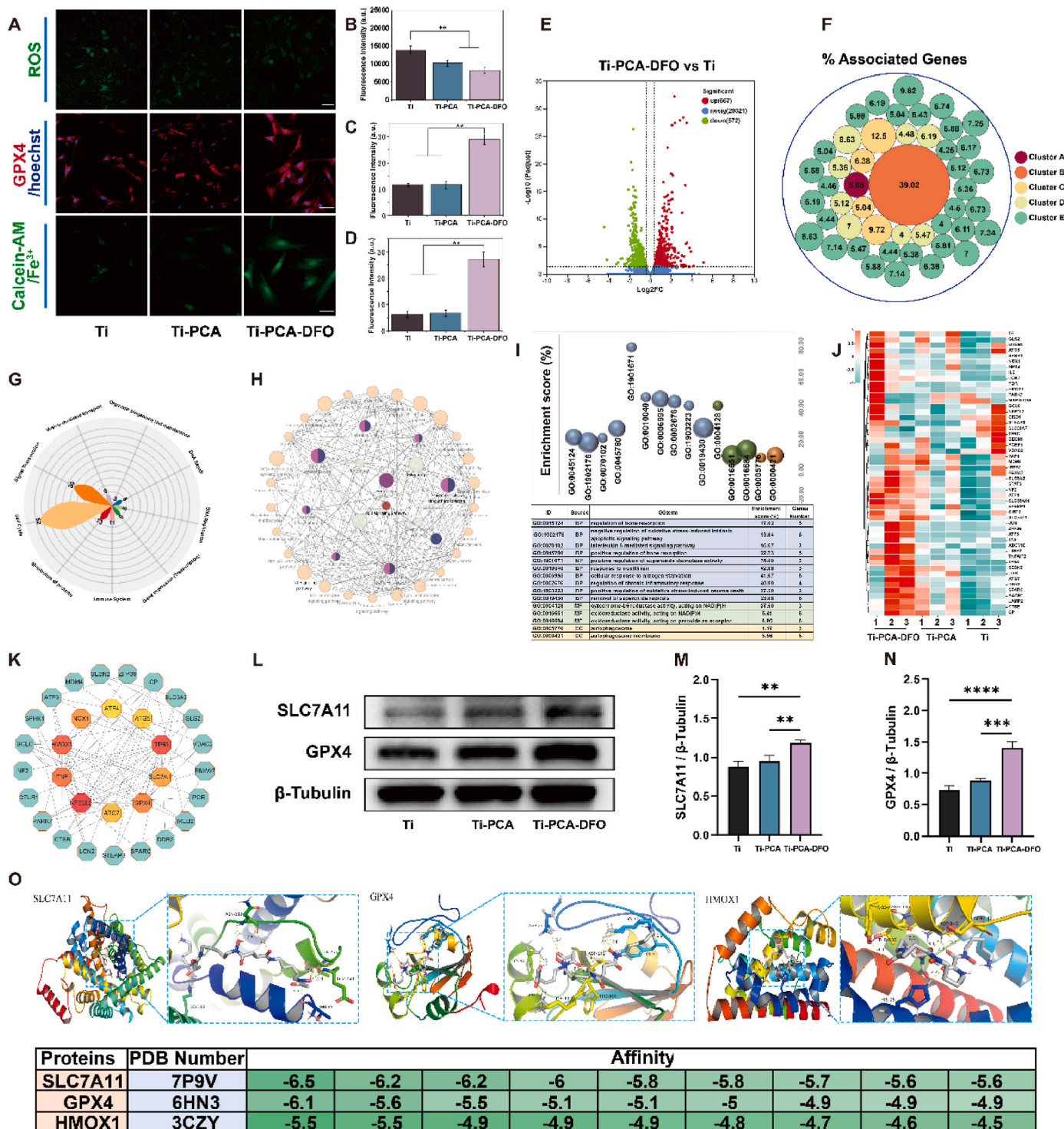
Fig. 7. (A) CLSM observation of ROS, GPX4, Clacein-AM; scale bar: 50 μm; The quantitative analysis of (B) ROS, (C) GPX4 and (D) Clacein-AM under conditioned culture; (E)Volcano plot of differential genes in Ti-PCA-DFO group compared with Ti group; (F) Cluster analysis of differentially expressed genes; (G) The main reactome pathways of differentially expressed genes; (H) KEGG and (I) GO enrichment analysis of DGs; (J) Heatmap of the DGS related to ferroptosis; (K) PPI network analysis of DGs and the core genes; Representative western blotting images (L) and quantitative analysis (M, N) of SLC7A11, GPX4, HMOX1; (O) The molecular docking of the core genes (SLC7A11, GPX4, HMOX1) and DFO. n = 3, *p <0.05, **p <0.01, ***p < 0.001, ****p < 0.0001.

high oxidative stress. In addition, NQO1 plays an important role in protecting endogenous antioxidants by maintaining reduced forms of ubiquinone and a-tocopherylquinone. The antioxidant pathway Keap1/Nrf2 is an important pathway regulating a series of antioxidant enzymes, so Ti-PCA and Ti-PCA-DFO may regulate oxidative stress in a high ROS environment through Keap1/Nrf2. Following the above conjecture, MSCs were co-cultured with Ti, Ti-PCA, and Ti-PCA-DFO respectively under high ROS and iron-overloaded microenvironment. Under stressful conditions, it was observed that the expression of activated KEAP1 in MSCs cells decreased following treatment with Ti-PCA and Ti-PCA-DFO compared to Ti, while the expression levels of NRF2, HMOX1, NQO1, and SOD were enhanced (Fig. 6K & L). It may be that Ti-PCA and Ti-PCA-DFO enhance the antioxidative capacity of MSCs. Subsequently, we employed the principles of spatial structure complementarity and energy minimization to investigate the interaction between CA and the active sites of KEAP1, NQO1, and HMOX1, while also determining their optimal binding mode. Consequently, we successfully identified the optimal binding position and strength of CA with KEAP1, NQO1, and HMOX1 by obtaining their respective binding conformations (Fig. 6M).

2.6. Evaluation of the ferroptosis of MSCs

As the main symbols of ferroptosis, ROS, GPX4, Calcein-AM, and JC-1 immunofluorescence staining in MSCs were performed. The increased SOD can inhibit ROS levels in MSCs. From Fig. 7A & **7B**, Ti-PCA and Ti-PCA-DFO have better ROS scavenging ability than Ti, especially for Ti-PCA-DFO under stressful conditions. GPX4 fluorescence in the Ti, Ti-PCA, and Ti-PCA-DFO groups increased gradually. As the most important antagonist molecule in ferroptosis, stronger immunofluorescence of GPX4 means a weaker ratio of ferroptosis in Ti-PCA-DFO (Fig. 7A & C). Meanwhile, Calcein-AM staining was used to indirectly characterize the changes of iron content in cells, because the fluorescence of Calcein-AM can be quenched by forming complexes with cytosolic iron. From laser confocal microscopy (CLSM) in Fig. 7A and D, the fluorescence intensity of MSCs in Ti-PCA-DFO was significantly higher than in other groups, indicating the minimal intracellular iron content of MSCs in Ti-PCA-DFO. Furthermore, a JC-1 kit was used to detect mitochondrial membrane potential. From the result of JC-1 (Figure S7), the Ti-PCA-DFO group has the biggest ratio of red/green fluorescence, indicating the minimal mitochondrial polarization and ferroptosis of MSCs. RNA sequencing results showed that contrasting with the Ti group, there are 1239 DGs in the Ti-PCA-DFO group, in which 677 genes were up-regulated and 572 genes were down-regulated (Fig. 7E). These DGs could be clustered into 5 main clusters (Fig. 7F), including the p53 signaling pathway (Cluster A), ferroptosis (Cluster B), autophagy and mitophagy (Cluster C), osteoclast differentiation and AGE-RAGE signaling pathway in diabetic complications (Cluster D), lipid peroxidation and oxidative stress (Cluster E). Wherein ferroptosis was most striking, whose ratio of associated genes was 39.02 %. The ferroptosis related genes from DGs included ATG5, ATG7, CP, GCLC, GPX4, HMOX1, MAP1LC3A, PCBP1, SLC39A14, SLC3A2, SLC7A11, STEAP3, TF, TFRC, TP53, and so on. Meanwhile, the reactome pathway (Fig. 7G) results showed that these DGs between Ti and Ti-PCA-DFO mainly enriched in the same 10 pathways to the Ti-PCA group, but the relative genes to cell cycle and metabolism of proteins increased by 6 and 2 respectively. KEGG results (Fig. 7H) showed that the main pathways of these DGs included ferroptosis, p53 signaling pathway, autophagy, mitophagy, osteoclast differentiation, TNF signaling pathway, HIF-1 signaling pathway, adipocytokine signaling pathway, etc. These pathways were closely related to apoptosis, ferroptosis, autophagy, and lipid peroxide. GO enrichment analysis results (Fig. 7I) showed that the most biological process in these DGs mainly focused on the regulation of bone resorption, regulation of oxidative stress, regulation of superoxide dismutase activity, response to iron (II) ion, etc. Most cellular components and molecular functions focused on autophagosome, cytochrome-b5 reductase activity, and oxidoreductase activity, respectively. The

results of GO enrichment proved that after coating with CA and DFO, iron overload-induced oxidative stress, lipid peroxidation, as well as iron responses were weakened. Based on the above results, we picked genes associated with ferroptosis from these DGs, and their expression was illustrated with a clustered heatmap in (Fig. 7J). To find the key genes, PPI analysis was adopted, by calculating the number of nodes between different proteins, the hub genes, TP53, HMOX1, NFE2L2, SLC7A11, GPX4, and NOX1 were picked out (Fig. 7K).

GPX4 is critical for the regulation of ferroptosis, and an important upstream protein of GPX4 is SLC7A11 [48]. SLC7A11 is the central transporter involved in ferroptosis suppression [49,50]. The up-regulation of SLC7A11 can promote indirectly the activity of GPX4 by increasing the cysteine metabolic pathway, leading to the growth of intracellular Cystine levels and the reduction of lipid peroxides, and ultimately inhibiting ferroptosis of MSCs [51,52]. Therefore, we then explored the effects of Ti, Ti-PCA, and Ti-PCA-DFO on the SLC7A11/GSH/GPX4 signaling pathway of MSCs in a microenvironment with high ROS and iron overload. Under stress conditions, SLC7A11/GSH/GPX4 expression levels were increased in MSCs treated with Ti-PCA and Ti-PCA-DFO compared with Ti (Fig. 7L– N). At the same time, after Ti-PCA-DFO treatment, the GSH content of MSCs increased significantly (Figure S8). Ti-PCA-DFO may enhance the resistance of MSCs to ferroptosis under high ROS and iron-overloaded microenvironment through the SLC7A11/GSH/GPX4 signaling pathway. We searched for the interaction between DFO and the active sites of SLC7A11, GPX4, and HMOX1 through the principle of spatial structure complementarity and energy minimization, as well as the optimal binding mode between them. The optimal binding position and binding strength of DFO and SLC7A11, GPX4, and HMOX1 were found, and their binding conformations were obtained (Fig. 7O).

2.7. Effects on osteogenic performance

The *in vivo* osteogenic effects of Ti, Ti-PCA, and Ti-PCA-DFO were evaluated by implanting into an osteoporosis animal model (Fig. 8A). As shown in Figure S9, the established osteoporosis rats in this work had a low number of bone trabeculae, bone structure, and low bone content, showing pathological features similar to those of osteoporosis models in past studies [53]. Compared to the Ti and Ti-PCA groups, the Ti-PCA-DFO group displayed a more compact trabecular arrangement and the highest amount of new bone growth after one month of implanting (Fig. 8B). Quantitative examination of the bone tissue surrounding implants supported that result (Fig. 8C). Bone mineral density (BMD), total volume ratio (BV/TV), and degree of anisotropy (DA) can reflect bone quality and strength. Trabecular number (Tb. N), trabecular thickness (Tb. Th), and trabecular separation (Tb. Sp) are the main indicators to evaluate the spatial morphology and structure of trabecular bone. The BMD, Tb. N, Tb. Th, BV/TV, and DA of the Ti-PCA-DFO group were significantly higher than that of the Ti group, suggesting Ti-PCA-DFO had higher bone strength. These results indicated that Ti-PCA-DFO can promote the formation of new bone and the microstructure of bone around the implant.

H&E and Masson staining (Fig. 8D & E) were used to analyze the formation of new bone around different implants. The results showed that thick bone-like tissue could be observed around the Ti-PCA-DFO implant. However, there was no tight connection between the implant and the host tissue in the Ti group. There was a cavity between the edge of the bone defect and the edge of the Ti implant. So, it was difficult to form dense new tissue, and the new bone structure in the Ti group was incomplete. After modification, more new bone tissues appeared around the implants, especially in the Ti-PCA-DFO group, and the implants fused well with the host. A large area of new bone tissue around the modified implants could be observed by magnifying images, and the new bone formation of the implant was thick. According to the results of Figs. 6 and 7, the important proteins of ferroptosis, the expression levels of GPX4, HMOX1, and SLC7A11 in the tissue were evaluated with
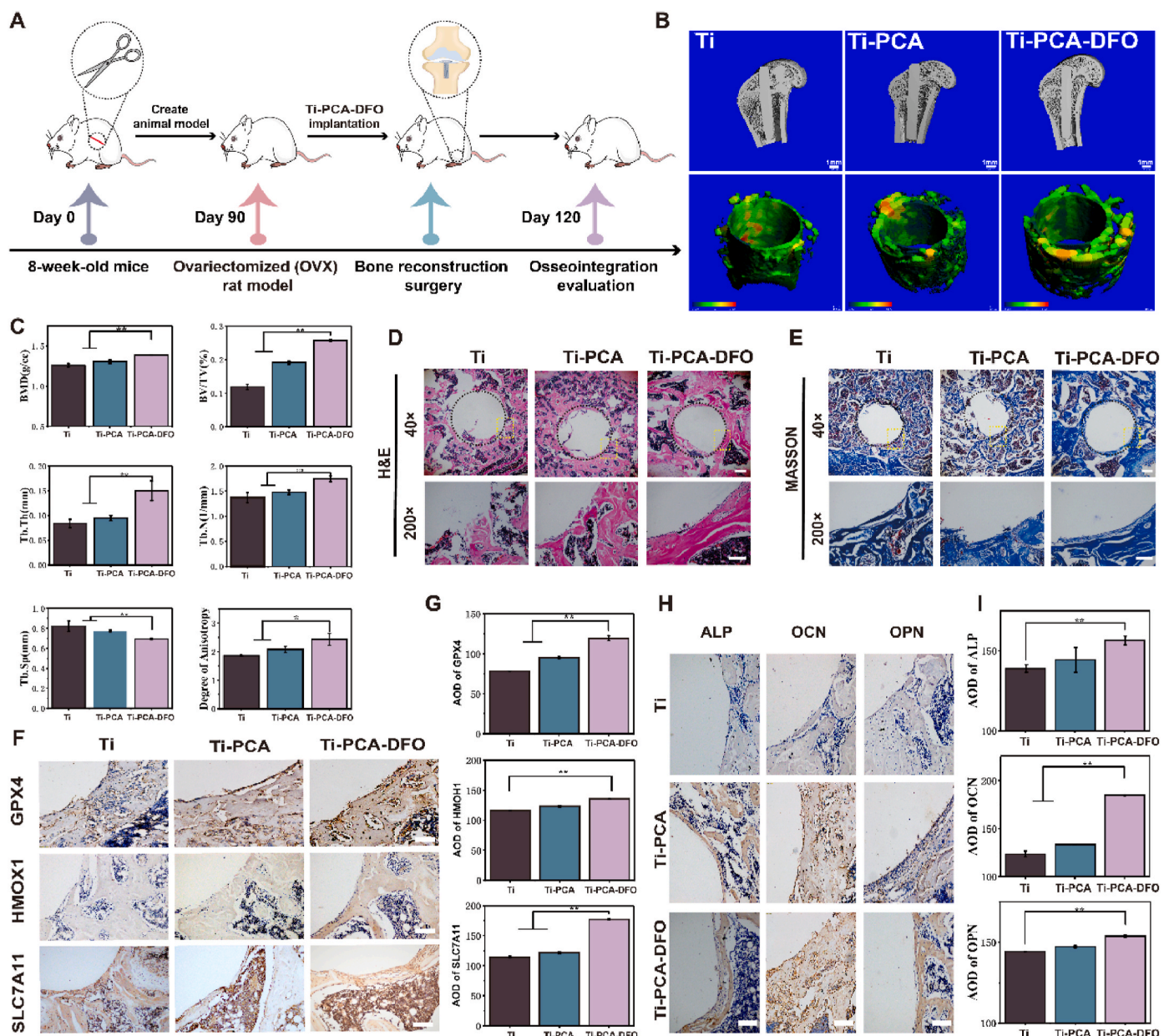
Fig. 8. Evaluation of *in vivo* bone formation. (A) Schematic illustration of *in vivo* implantation. (B) Micro-CT images of new bone formation and trabecular thickness around different implants, scale bar: 1 mm; Colors from green to red represent changes in trabecular thickness from thin to thick. (C) Quantitative analysis of bone mineral density (BMD), New bone volume per total volume (BV/TV), the number of trabeculae (Tb. N), trabecular thickness (Tb. Th), trabecular bone separation (Tb. Sp) and anisotropic thickness (DA) around different implants. (D) H&E staining and (E) Masson staining of new bone around implants, the black circle shows the implant's edge and osteogenic position, and the yellow box shows the local enlargement position, 40 × scale bar: 500 μm, 200 × scale bar: 100 μm. (F) Immunohistochemical staining and (G) Average optical density of GPX4, HMOX1, and SLC7A11, scale bar: 100 μm. (H) Immunohistochemical staining and (I) average optical density of ALP, OCN, and OPN of new bone around implants, scale bar: 100 μm. n = 5, *$p < 0.05$, **$p < 0.01$.

immunohistochemical staining (Fig. 8F) and average optical density (Fig. 8G). Which, the positive expressions of GPX4 and SLC7A11 in Ti-PCA-DFO were significantly higher than the other group, especially for the Ti group. As for HMOX1, although no statistical differences were found between Ti-PCA and Ti, the expression of Ti-PCA-DFO was significantly higher than that of the Ti group. As the recognized markers of osteogenesis, the expression levels of ALP, OCN, and OPN proteins in the tissues were detected by immunohistochemical staining (Fig. 8H). ALP, OCN, and OPN are enzyme proteins secreted by osteoblasts, which are one of the most commonly used indicators to evaluate the secretory function of osteoblasts. As shown in Fig. 8I, ALP, OCN, and OPN were significantly positive in the Ti-PCA-DFO group, suggesting higher expression levels of the three proteins. The results of Micro-CT, H&E

staining, Masson staining, and immunohistochemical staining proved that contrasting with pure Ti, the Ti-PCA and Ti-PCA-DFO groups could inhibit ferroptosis greatly, thus could increase bone mineral density and spatial structure of trabecular bone around the implants in the osteoporotic bone defect model.

3. Discussion

Normally, the organism can effectively counteract iron toxicity and maintain sufficient iron required for hemoglobin synthesis and basic metabolic functions, while also regulating its concentration, storage, and distribution within tissues [54–56]. Some work has demonstrated the effects of iron deficiency on the capacity of progenitor cell

differentiation pathways. Moderate iron can prove osteoblast differentiation ability [57,58]. However, postmenopausal women, in addition to estrogen deficiency, may also exhibit iron accumulation, leading to bone loss and developing postmenopausal osteoporosis (PMOP) [9,59]. Excess iron can potentially catalyze free radicals, leading to cellular lipid peroxidation and damage to membrane function, ultimately resulting in the occurrence of PMOP [43,60,61]. Osteoporosis is a chronic metabolic disease with a high incidence of fractures and requires the support of a fixation system. Especially for postmenopausal osteoporosis patients, implantable fixation systems are long-term or even permanent implants [3]. In any case, postoperative implant loosening remains a serious challenge for patients with osteoporosis. Postmenopausal women tend to let more iron accumulation in the body, producing oxidizing substances that break the balance in the bone, causing bone loss and osteoporosis [6,14]. This may result in poor binding ability to the implant.

To investigate the correlation between iron overload and osteoporosis, we initially analyzed the differentially expressed miRNAs in plasma samples from postmenopausal patients with and without osteoporosis, retrieved from the GEO database. By enrichment analysis of these miRNAs, the main biological processes and the main reactome pathways occurring in the PMOP plasma (Fig. 1B) were discovered. Most miRNAs were enriched to four reactome pathways, signal transduction, immune system, metabolism, and metabolism of proteins. Moreover, the most target genes (TP53, TNFSF11, RUNX2, WNT3A, COL1A1, COL1A2) of these different miRNAs were related to bone formation and resorption (Fig. 1). Some literature showed that iron metabolism is crucial for bone homeostasis [55,60]. MSCs are the main source of bone formed in the adult bone marrow and play a key role in bone homeostasis and aging [62,63]. Therefore, we further explored the effect of excess iron accumulation on MSCs during the pathological process of PMOP. We used a culture medium with different iron concentrations to culture MSCs. The results showed that moderate Fe^{3+} could promote cell growth and osteogenic activity, but excessive Fe^{3+} would inhibit cell viability and ALP activity (Fig. 2A & B). Moreover, genetic responses of MSCs from RNA sequencing revealed an iron metabolism mechanism. Among them, the significantly up-regulated genes were SPP1, NQO1, HMOX1, GSTA1, SLC19A1, GSTP1, etc (Fig. 2E–H), which are the key genes related to oxidative stress and ferroptosis. The results of in vitro cell experiments (Calcein-AM, JC-1, and GPX4 immunofluorescence staining) and the genomic characteristics suggested that excessive iron may activate oxidative stress, fatty acid metabolism, and ferroptosis pathways, which would lead to MSCs ferroptosis and reduction of osteogenesis (Fig. 2).

Ferroptosis is an iron-dependent regulated form of cell death, which is caused by iron-dependent lipid peroxidation [64]. Based on the two main conditions of ferroptosis occurrence, iron overload, and lipid peroxidation, in this work, we designed a novel CA and DFO coating for the regulation of ferroptosis. CA could form PCA film on Ti by the metal coordination and the auto-oxidation triggered radical chain-growth polymerization. Then, DFO was grafted onto PCA film via the dynamic borate ester bond. Under normal physiological conditions, DFO could promote angiogenesis and osteogenesis. However, under the pathological environment of high oxidative stress in osteoporosis, DFO could complex iron and achieve ROS-responsive release through the breakage of borate ester bond (Fig. 4G), thereby reducing the iron concentration around the implant. Meanwhile, the remained caffeic acid coating could reduce the oxidative stress level and lipid peroxidation around the implant.

From Figs. 1 and 2, iron overload leads to the increase of intracellular iron, and increase the expression of ferroptosis-related genes and proteins. Wherein, the KEAP1/Nrf2/HMOX1 pathway was activated may be that cells are stimulated to activate antioxidant signaling pathways for self-protection [65]. Moreover, impaired mitochondrial transfer of osteoblasts can alter glutathione metabolism. Once excess iron enters the cell, it can cause metabolic problems. Glutathione reduces Fe^{3+} to Fe^{2+} [66,67]. In this work, after coating with CA, the samples (Ti-PCA and Ti-PCA-DFO) inhibited expressions of KEAP1, and up-regulated the

levels of NRF2, HMOX1, NQO1 and SOD (Fig. 6K & L), indicating the activation of KEAP1/Nrf2/HMOX1 pathway. The activation of KEAP1/NRF2/HMOX1 signal can protect cells from oxidative stress [68, 69]. Ti-PCA-DFO activated the NRF2-dependent cellular defense mechanism, and NRF2 was released from KEAP1 and translocated to the nucleus, thereby increasing the expression of HMOX1, NQO1, and SOD, protecting MSCs from cytotoxicity and apoptosis induced by H_2O_2 and high iron environment. Ti-PCA and Ti-PCA-DFO reduced oxidative stress in MSCs and regulated cell cycle, proliferation, apoptosis, and metabolism (Figs. 5 and 6). Therefore, activation of the KEAP1/NRF2/HMOX1 pathway demonstrated that Ti-PCA-DFO enhanced the defense role of MSCs against oxidative stress and reduced lipid peroxidation levels around Ti-PCA-DFO.

From the points of the formation of lipid peroxides and the main marker of ferroptosis, in the conditioned medium with high ROS and high iron content, ferroptosis may occur in all groups. In the Ti-PCA-DFO group, the formed DFO-Fe ions complex could be released under high ROS conditions, leading to a decrease in iron ion concentration and the induction of ferroptosis in MSCs surrounding the implant (Fig. 7). Furthermore, the residual caffeic acid coating could mitigate ROS and lipid peroxide formation, also contributing to a reduction in the ferroptosis of MSCs around the implant. Meanwhile, the expression of SLC7A11 and GPX4 was increased, implying Ti-PCA-DFO can activate the SLC7A11/GSH/GPX4 signaling axis, prevent glutathione depletion, and promote the reduction of lipid ROS, thereby inhibiting ferroptosis [70]. In vivo results showed that high oxidative stress and iron levels in postmenopausal osteoporosis may lead to ferroptosis of MSCs, thereby affecting osteogenesis. But, after coating with caffeic acid and DFO, the level of oxidative stress and lipid peroxidation around the Ti implant (Ti-PCA and Ti-PCA-DFO) could be decreased obviously, which will benefit to inhibit the formation of osteoclasts and bone resorption. Moreover, after being grafted with DFO, Ti-PCA-DFO could inhibit the ferroptosis of MSCs and promote osteogenesis by reducing the iron overload around the implant (Figs. 8 and 9).

In conclusion, we tried to reveal the mechanism of postmenopausal osteoporosis based on its biological information and confirmed the effect of iron overload on pmop through subsequent transcriptome sequencing and cell experiments. Based on the above studies, the design of titanium implants that meet the special needs of pmop is essential for bottom-up material design. In this way, we can classify according to the specific circumstances of disease occurrence and differentiate the design of intelligent biomaterials to be more suitable for the needs of individuals, which is in line with the concept of precision medicine. This paper demonstrates the usability and potential of "Database + Material design" to improve material design.

4. Conclusion

PMOP is a common disease in elderly women after menopause. Excepting for the decrease of estrogen level, many factors such as oxidative stress and iron overload also play important roles in the occurrence and development of PMOP. MiRNA analysis of plasma samples from postmenopausal and non-osteoporosis patients showed that ferroptosis is one of the important pathogenesis of PMOP. The moderate Fe^{3+} could promote cell growth and ALP activity. However, the excessive Fe^{3+} may cause ferroptosis of MSCs, resulting in the decrease of cytoactive and osteogenesis. Therefore, we designed novel CA nanospheres and DFO film on the Ti implant surface for the regulation of ferroptosis. Under the high ROS and excessive iron environment of PMOP, the grafted DFO could achieve ROS responsive release, which could chelate the excessive iron and decrease the iron overload in MSCs around the implant. Meanwhile, the remaining CA coating could reduce the oxidative stress level and lipid peroxidation around the implant. In conclusion, we designed an intelligent titanium implant (Ti-PCA-DFO) based on the mechanism of osteoporosis, which can alleviate iron overload and oxidative stress of PMOP and improve the integration
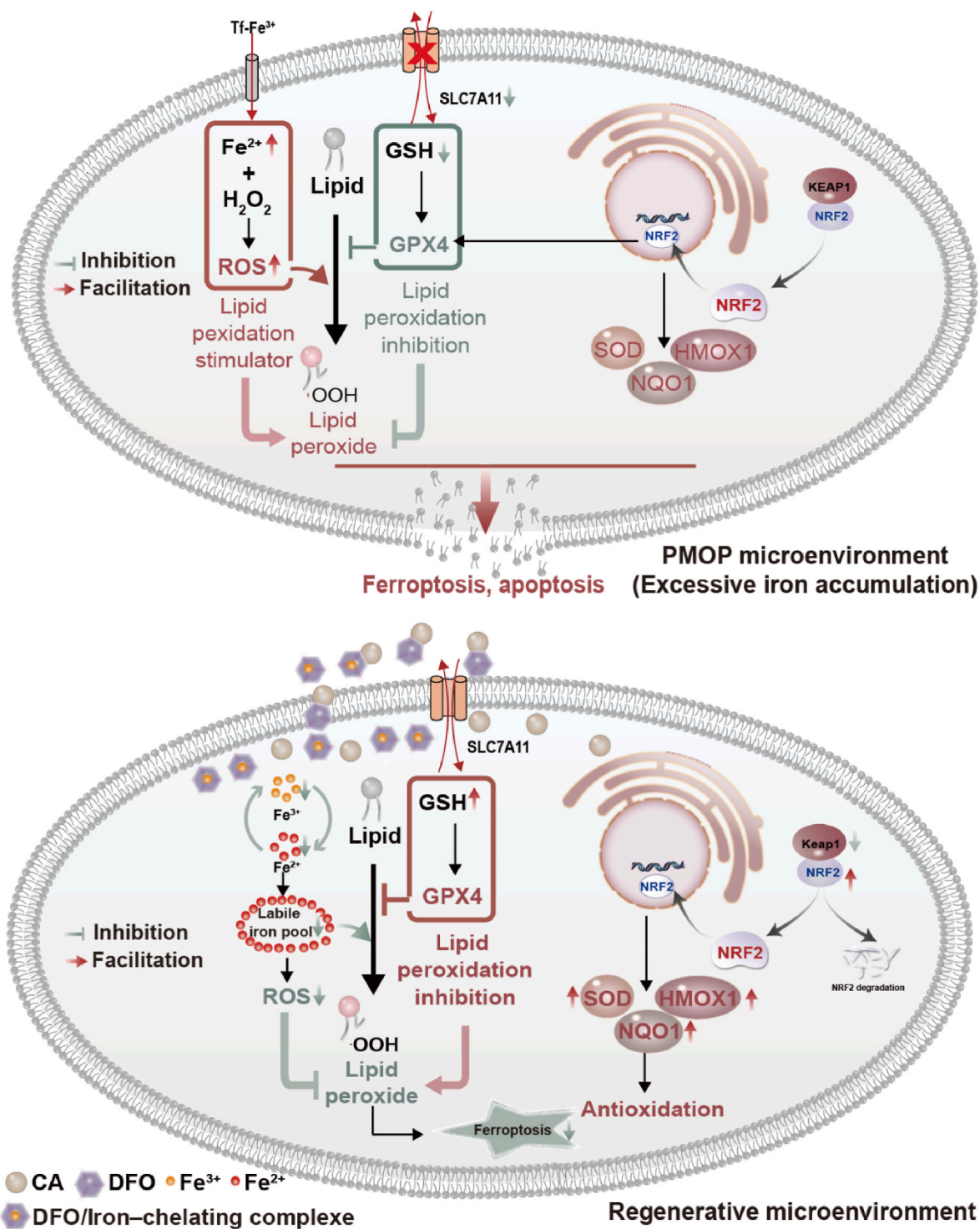
Fig. 9. Schematic diagram of the molecular mechanism of Ti-PCA-DFO in PMOP.

ability of bone and implant. This offers a framework for future smart biomaterial design, leveraging disease databases to develop optimal biomaterials for specific pathologies.

5. Experimental section

Materials. Commercial Ti foil rods were provided by Alfa Awsar Co. (Tianjin, China) and Northwest Institute for Non-ferrous Metal Research (Shaanxi, China). Caffeic acid (CA) was obtained from Meryer Chemical Technology Co. Ltd (Shanghai, China). 3-carboxyphenylboric acid (3-

CPBA) was supplied by Aladdin Biochemical Technology Inc. (Shanghai, China). Deferoxamine mesylate (DFO) was bought from Yien Chemistry Technology Co., Ltd. (Shanghai, China). C11 BODIPY 581/591 probe was purchased from Iboteck Biotechnology Co. Ltd. (Wuhan). Cy3 Goat Anti-Rabbit IgG (H + L), FITC Goat Anti-Mouse IgG (H + L), and GPX4 were purchased from Biotechnology Co. Ltd. The primary antibodies of KEAP1, NRF2, HMOX1, NQO1, SOD, GPX4 and β-Tubulin were purchased from Proteintech Group, Inc (China). The primary antibody of SLC7A11 was purchased from Affinity Biosciences. Ltd (China). ALP and BCA assay kits were purchased from Beyotime Biotechnology Co. Ltd.

(China).

Bioinformatics analysis of osteoporosis. GSM246440-GSM246451 were downloaded from the GEO database and named A-1 to A-6 for the osteoporosis sample group and B-1 to B-6 for the normal sample group. Gene ontology (GO), Kyoto Encyclopedia of Genes and Genomes (KEGG) enrichment analysis, and protein interaction network (PPI) analysis were performed by Metascore, String, and Cytoscope.

Synthesis of CPBA-DFO. 3-CPBA (33.2 mg, 0.2 mmol) was dissolved in 5 ml DMF and stirred. Then 1- (3-dimethylaminopropyl) -3-ethyl-carbodiimide hydrochloride (EDC, 31 mg, 0.2 mmol) and 1-hydroxybenzotriazole (HOBT, 27 mg, 0.2 mmol) were added to the solution for activation for 1 h. Then deferoxamine mesylate (DFO, 150.6 mg, 0.2 mmol) was added, the pH was adjusted to 8.4 with triethanolamine (TEA), and the mixture was stirred for 24 h at room temperature. Finally, the crude product was obtained by rotary steaming, ethanol washing several times, and centrifugation, which was used in a vacuum freeze dryer and vacuum dried for 48 h to obtain CPBA-DFO powder.

Fabrication of ROS-responsive coating on Ti surface. The titanium platinum was cut into square pieces (1×1 cm^2), and cleaned with surfactant, alcohol, and two steamed water for 15 min. The cleaned samples were dried in the oven for subsequent experimental use. Then the Ti substrate was incubated with CA solution (100 μM) in the dark for 12 h, named Ti-PCA. CPBA-DFO (1 mg/mL) was suspended onto the Ti-PCA surface to prepare a ROS-responsive coating, and the sample was named Ti-PCA-DFO. (1 mg/mL). Nuclear magnetic resonance (NMR) spectroscopy (AV500 MHz, Bruker, Switzerland), Fourier transform infrared spectroscopy (FTIR), and ultraviolet–visible (UV–Vis) spectrophotometer (PECORD®210 PLUS, Analytikjena, German) were subjected to confirm the successful synthesis of CPBA-DFO conjugates. X-ray photoelectron spectroscopy (XPS) (Model PHI 5400, PerkinElmer, USA), Atomic Force Microscopy (AFM) (MFP-3D-BIO, USA), and field emission scanning electron microscopy (FE-SEM, FEINova Nano SEM, Phillips Co., Holland) were utilized to observe the micro-morphology and roughness of specimens.

Drug release. PBS buffer (pH 7.4) and H$_2$O$_2$ (200 μM) were used as the release medium for the Ti-PCA-DFO drug release assay *in vitro*. Ti-PCA-DFO was placed in PBS buffer or H$_2$O$_2$ (200 μM) solution containing FeCl$_3$ (500 μM). At different time points (1 h, 2 h, 6 h, 12 h, 24 h, 36 h, 48 h, 72 h, 96 h, 120 h), 20 μL of the solution was taken and measured by Ultraviolet–visible spectrophotometry (NanoDrop One, ND-ONE-W, Thermo, USA) at a wavelength of 430 nm. Ammonium ferric citrate (100 μM) was added, and absorbance values were determined using a UV–Vis spectrophotometer at a wavelength of 430 nm. Subsequently, the same volume of the corresponding PBS solution was added to the original solution. Drug release was determined according to the standard curve.

Iron detection assay. To detect the iron chelating ability of Ti-PCA-DFO, Ti-PCA-DFO was placed in Fe^{3+} solution (100 μM). The iron concentration in the solution was quantified with an inductively coupled plasma series mass spectrometer (ICP-MS-MS, PerkinElmer, Switzerland).

Cell culture. MSCs suspensions were obtained from SD rat bone marrow under sterile conditions. The suspension of BMSCs was cultured in a cell incubator (37 °C, 5 % CO$_2$) and recorded as P$_0$ generation. The medium was changed every 48 h, and when the cells proliferated to cover about 90 % of the culture flask area, the cells were passaged. The third-generation cells (P$_3$) with good growth patterns were selected for subsequent *in vitro* cell experiments. Unless otherwise specified, MSCs were cultured with FAC solution (0, 100 μM), or cultured on Ti, Ti-PCA, and Ti-PCA-DFO in a medium containing 100 μM FAC and 100 μM H$_2$O$_2$ for 4 days.

The cell viability assay. MSCs (2×10^4 cells/well) were incubated in the plates overnight, and cultured with FAC solution (0, 50, 100, 200, 400, 500, 600 μM) for 4 days. Subsequently, the medium was removed and CCK8 solution was added and incubated at 37 °C in the dark for 2 h. MSCs (2×10^4 cells/well) were cultured on Ti, Ti-PCA, and Ti-PCA-DFO for 4 and 7 days. The medium used contained 100 μM FAC and 100 μM H$_2$O$_2$. CCK8 solution was added and incubated in the dark for 2 h. FDA/PI dye was added to observe the survival and death of the cells by CLSM.

Apoptosis and cell cycle. MSCs were incubated in the plates overnight, and cultured with FAC solution (0, 100, 200 μM) and DFO solution (10 μM) for 4 days. In a medium containing 100 μM FAC and 100 μM H$_2$O$_2$, MSCs were cultured on Ti, Ti-PCA, and Ti-PCA-DFO for 4 days, respectively. After the cells were washed with PBS, the cells were suspended again with 200 μL binding buffer. Annexin V-FITC (5 μL) and propidium iodide (10 μL) were added, and cell apoptosis was detected by flow cytometer. The cells that measure cell cycles were first immobilized in 70 % precooled ethanol overnight, then 100 μL of RNase A solution was added to the cell precipitate at 37° for 30 min. PI staining solution (400 μL) was added and incubated for 30 min. The cells were detected by flow cytometry.

Cytoskeleton assay. MSCs were cultured on Ti, Ti-PCA, and Ti-PCA-DFO for 24 h. The medium used contained 100 μM FAC and 100 μM H$_2$O$_2$. Cells on the surface of the samples were fixed with 4 % paraformaldehyde after the culture medium was first removed. FITC-amanita phalloides solution (200 μL) was added and incubated at 37 °C in the dark for 30 min. After washing off the staining solution, Hoechst 33258 staining solution was added and incubated for 15 min. The cells were observed by CLSM.

Osteogenesis-related assay. Alkaline phosphatase (ALP) and Collagen activity were quantitatively detected. Mineralization levels were measured using the alizarin red method. MSCs were incubated in the plates overnight, and cultured with FAC solution (0, 50, 100, 200, 400, 500, 600 μM) for 7 days. MSCs were cultured on Ti, Ti-PCA, and Ti-PCA-DFO for 7 days. The medium used contained 100 μM FAC and 100 μM H$_2$O$_2$. Then the medium was removed and 1 % Triton X-100 was added to lysis the cells. BCA kit and ALP kit were used to measure the total protein and ALP activity in the cells. The specific steps of collagen activity detection are: 4 % paraformaldehyde was used to immobilize cells after the medium was removed first. Next, Sirius red staining solution (200 μL) was added and stained for 60 min. Afterward, the images were documented on a digital camera. To quantify the secretion level, 200 μL NaOH (0.1 M) was supplemented lasting 10 min. Ultimately, the 540 nm OD value of the supernatant was measured. The specific steps of mineralization are: 4 % paraformaldehyde was used to immobilize cells after the medium was removed first. Next, alizarin red staining solution (200 μL) was added and incubated at 37 °C for 60 min for staining. Afterward, the images were documented on a digital camera. As for the next quantitation, acetic acid with a volume ratio of 10 % was added and incubated for 30 min with shaking. The cells were then treated in a water bath at 85 °C for 10 min and centrifuged for 15 min (12000 rpm). In the end, an equal volume of 10 % ammonia solution was added to the supernatant and its OD value at 405 nm was measured with a microplate reader.

MSCs RNA sequencing and results analysis. To explore the Iron metabolism mechanism and the effects of modified titanium on cell gene expression. MSCs were incubated in the plates overnight, and cultured with FAC solution (0, 100 μM) for 4 days. In a medium containing 100 μM FAC and 100 μM H$_2$O$_2$, MSCs were cultured on Ti, Ti-PCA, and Ti-PCA-DFO for 4 days for RNA sequencing. Specifically speaking, extracted RNA was sequenced through the Illumina Novaseq 6000 sequencing platform of Magor Biomedical Technology Co.Ltd (Shanghai, China). Each set was repeated three times. After setting the significance threshold ($|Log_2FC| \geq 1.5$, P < 0.05), GO/KEGG functional pathway analysis was performed.

Calcein-AM assay. Calcein-AM assay is a method to evaluate intracellular iron levels. Calcein-AM can form complexes with cytosolic iron and quench fluorescence. MSCs were cultured with FAC solution (0, 100 μM), or cultured on Ti, Ti-PCA, and Ti-PCA-DFO in a medium containing 100 μM FAC and 100 μM H$_2$O$_2$ for 24 h. The cells were stained with Calcein-AM and observed by CLSM.

Detection of GPX4 protein. The specific procedures of GPX4

staining were as follows: cells on the surface of the sample fixed with 4 % paraformaldehyde. And discarding the liquid and lysing the cells with 0.5 % Triton X-100. Then the cells were blocked with a blocking solution for 1 h. After washing with PBS, the cells were incubated with GPX4 antibody for 12 h at 4 °C. FITC Goat Anti-Mouse IgG (H + L) was discarded and stained for 10 min, and then observed by CLSM.

Mitochondrial membrane potential. JC-1 kit was used to detect mitochondrial membrane potential. After 24 h of MSCs culture, 200 μL JC-1 working solution was added and cultured in a 37 °C incubator for 20 min. After the staining solution was removed and washed with PBS, the cells were observed by laser confocal microscopy.

Lipid reactive oxygen species (Lipid ROS) detection and reactive oxygen species (ROS) detection. MSCs were seeded on Ti, Ti-PCA, and Ti-PCA-DFO overnight and incubated with 100 μM FAC and 100 μM H_2O_2 for 24 h. C11 BODIPY 581/591 storage solution was added and incubated for 60 min to detect Lipid ROS. Flow cytometry was used for detection. DCFH-DA was added to the supernatant of each sample and incubated in the dark to detect ROS. Then qualitative and quantitative ROS were detected by CLSM.

Superoxide dismutase (SOD) activity and Malondialdehyde (MDA). MSCs were seeded on Ti, Ti-PCA, and Ti-PCA-DFO overnight and incubated with 100 μM FAC and 100 μM H_2O_2. The SOD enzyme detection kit was used for detection. MDA was detected by a malondialdehyde kit.

Western blot analysis. In a medium containing 100 μM FAC and 100 μM H_2O_2, MSCs were cultured on Ti, Ti-PCA, and Ti-PCA-DFO for 4 days for Western blot analysis. Protein was extracted from each group and then electrophoresis, transmembrane, and protein blocking. After incubated with the antibodies of KEAP1, NRF2, HMOX1, NQO1, SOD, SLC7A11, GPX4, and β-Tubulin, secondary antibodies labeled by horseradish peroxidase were slowly shaken and incubated for 1 h. The PVDF membranes were developed by instrument. (VersaDoc MP 4000 Bio-Rad, USA).

Detection of GSH. To detect gsh content, MSCs were cultured on Ti, Ti-PCA, and Ti-PCA-DFO for 4 days in a medium containing 100 μM FAC and 100 μM H_2O_2, respectively. Specific steps, according to the micro-reduced glutathione assay kit instructions to detect the gsh content.

SD rat Model construction and implantation *in vivo*. Female Sprague-Dawley rats (~200g, 8 weeks of age) were provided by Chongqing Medical University. All animal experiments were approved by the Ethics Committee of Chongqing University [CQU-IACUC-RE-202205-001]. They were randomly divided into Ti, Ti-PCA, and Ti-PCA-DFO groups (n = 5). According to the previous study, all rats were treated with bilateral ovariectomy and fed for 3 months to establish an osteoporosis model. Subsequently, different Ti implants were implanted into the femoral epiphysis of osteoporotic rats for 1 month.

Micro-CT. The remaining osteoporotic rats were sacrificed after 1 month, and their femurs were removed. The collected femur samples were fixed in a 4 % polyformaldehyde solution to detect bone mass and bone maturity around different implants; Micro-CT was used to scan the bone tissue around the implant. The analysis area of bone formation was set as a radius of 0.4 mm around the implant. CTAn software was used to quantitatively analyze the new bone volume/total volume ratio (BV/TV), trabecular number (Tb. N), trabecular thickness (Tb. Th), and trabecular space (Tb. Sp).

H&E staining and Masson staining. The sections were deparaffinized according to the instructions of the H&E staining and Masson staining kit. Next, the sections are dyed according to the instructions of the staining kit. The sectioned tissues were dehydrated by gradient dehydration with ethanol and xylene. The sections were sealed with neutral resin, dried, and observed under a microscope.

Immunohistochemical staining. Immunohistochemical staining was used to detect the expression of alkaline phosphatase (ALP), osteocalcin (OCN), osteopontin (OPN), glutathione peroxidase 4 (GPX4), heme oxygenase 1 (HMOX1) and cystine/glutamate antiporter (SLC7A11). After deparaffinization and protein blocking, the primary

antibodies (1:200) were added and incubated at 4 °C overnight. Then, a diluent of secondary antibody (1:200) was added and incubated at room temperature for 60 min. A Hematoxylin staining solution was added for staining. After the section was sealed, the microscope was used for observation and quantitation.

Statistical analysis. Data were presented in the form of means ± standard deviation. One-way analysis of variance (ANOVA) together with the students' test were exerted to verify the statistical significance of the data, while OriginPro and Graphpad prism were utilized for statistical analysis. P value less than 0.05 was considered statistically significant. * and ** were represented $P < 0.05$ and $P < 0.01$ respectively.

Data availability

Data will be made available on request.

Ethics approval and consent to participate

All animal experiments were approved by the Ethics Committee of Chongqing University [CQU-IACUC-RE-202205-001].

CRediT authorship contribution statement

Yulu Yang: Writing – original draft, Visualization, Validation, Software, Methodology, Investigation, Formal analysis, Data curation, Conceptualization. **Xianhui Zhang:** Writing – original draft, Visualization, Methodology, Data curation, Conceptualization. **Yao Yang:** Visualization, Software, Methodology, Formal analysis, Data curation. **Pengfei Gao:** Visualization, Methodology, Formal analysis, Data curation. **Wuzhe Fan:** Visualization, Methodology, Formal analysis, Data curation. **Tao Zheng:** Visualization, Software, Investigation, Formal analysis. **Weihu Yang:** Writing – review & editing, Validation, Supervision, Resources, Project administration, Methodology, Investigation, Funding acquisition. **Yu Tang:** Writing – review & editing, Supervision, Resources, Methodology, Investigation. **Kaiyong Cai:** Writing – review & editing, Validation, Supervision, Resources, Project administration, Methodology, Funding acquisition, Conceptualization.

Declaration of competing interest

The authors declare that they have no known competing financial interests or personal relationships that could have appeared to influence the work reported in this paper.

Acknowledgments

Appendix ASupplementary data

Supplementary data to this article can be found online at https://doi.org/10.1016/j.bioactmat.2024.07.024.

References

[1] R. Eastell, T.W. O'Neill, L.C. Hofbauer, B. Langdahl, I.R. Reid, D.T. Gold, S. R. Cummings, Postmenopausal osteoporosis, Nat. Rev. Dis. Prim. 2 (2016).

[2] D.M. Black, C.J. Rosen, Postmenopausal osteoporosis, N. Engl. J. Med. 374 (3) (2016) 254–262.

[3] C. von Ruedena, P. Augat, Failure of fracture fixation in osteoporotic bone, Injury 47 (2016) S3–S10.

[4] M. Kaur, K. Singh, Review on titanium and titanium based alloys as biomaterials for orthopaedic applications, Mat. Sci. Eng. C-Mater 102 (2019) 844–862.

[5] T. Takizawa, N. Nakayama, H. Haniu, K. Aoki, M. Okamoto, H. Nomura, M. Tanaka, A. Sobajima, K. Yoshida, T. Kamanaka, K. Ajima, A. Oishi, C. Kuroda, H. Ishida, S. Okano, S. Kobayashi, H. Kato, N. Saito, Titanium fiber plates for bone tissue repair, Adv. Mater. 30 (4) (2018).

[6] G. Dvorak, C. Arnhart, S. Heuberer, C.D. Huber, G. Watzek, R. Gruber, Peri-implantitis and late implant failures in postmenopausal women: a cross-sectional study, J. Clin. Periodontol. 38 (10) (2011) 950–955.

[7] A. Temmerman, L. Rasmusson, A. Kuebler, A. Thor, J. Merheb, M. Quirynen, A prospective, controlled, multicenter study to evaluate the clinical outcome of implant treatment in women with osteoporosis/osteopenia: 5-year results, J. Dent. Res. 98 (1) (2019) 84–90.

[8] J. Jian, E. Pelle, X. Huang, Iron and menopause: does increased iron affect the health of postmenopausal women? Antioxidants Redox Signal. 11 (12) (2009) 2939–2943.

[9] B. Chen, G.-F. Li, Y. Shen, X. Huang, Y.-J. Xu, Reducing iron accumulation: a potential approach for the prevention and treatment of postmenopausal osteoporosis, Exp. Ther. Med. 10 (1) (2015) 7–11.

[10] X. Fang, H. Ardehali, J. Min, F. Wang, The molecular and metabolic landscape of iron and ferroptosis in cardiovascular disease, Nat. Rev. Cardiol. 20 (1) (2023) 7–23.

[11] S. Lakhal-Littleton, Ferroportin mediated control of iron metabolism and disease, Blood 128 (2016) SCI–21.

[12] K.-a. Ishii, T. Fumoto, K. Iwai, S. Takeshita, M. Ito, N. Shimohata, H. Aburatani, S. Taketani, C.J. Lelliott, A. Vidal-Puig, K. Ikeda, Coordination of PGC-1β and iron uptake in mitochondrial biogenesis and osteoclast activation, Nat. Med. 15 (3) (2009) 259–266.

[13] Q. Ru, Y. Li, W. Xie, Y. Ding, L. Chen, G. Xu, Y. Wu, F. Wang, Fighting age-related orthopedic diseases: focusing on ferroptosis, Bone Res. 11 (1) (2023).

[14] C. Hui, Z. Huimei, H. Weiting, Z. Heng, Iron accumulation and its impact on osteoporotic fractures in postmenopausal women, J. Zhejiang Univ. - Sci. B 24 (2023) 301.

[15] G.M. Malcolm, E.M. Alan, M.P. Jacquelyn, A.K. Peter, H.O.B. Sarah, R. Toby, L. Michelle, S.L. Barbara, The relationship between heavy menstrual bleeding, iron deficiency, and iron deficiency anemia, Am. J. Obstet. Gynecol. 229 (2023).

[16] H. Zhang, A. Wang, G. Li, Q. Zhai, Z. Huang, X. Wang, Z. Cao, L. Liu, G. Liu, B. Chen, K. Zhu, Y. Xu, Y. Xu, Osteoporotic bone loss from excess iron accumulation is driven by NOX4-triggered ferroptosis in osteoblasts, Free Radical Biol. Med. 198 (2023) 123–136.

[17] A. Ajoolabady, H. Aslkhodapasandhokmabad, P. Libby, J. Tuomeilehto, G.Y.H. Lip, J.M. Penninger, D.R. Richarrdson, D. Tang, H. Zhou, S. Wang, D.J. Kionsky, G. Kroemer, J. Ren, Ferritinophagy and ferroptosis in the management of metabolic diseases, Trends Endocrinol. Metabol. 32 (7) (2021) 444–462.

[18] Z. Gao, Z. Chen, Z. Xiong, X. Liu, Ferroptosis - a new target of osteoporosis, Exp. Gerontol. 165 (2022).

[19] Z. Jiang, H. Wang, G. Qi, C. Jiang, K. Chen, Z. Yan, Iron overload-induced ferroptosis of osteoblasts inhibits osteogenesis and promotes osteoporosis: an in vitro and in vivo study, IUBMB Life 74 (11) (2022) 1052–1069.

[20] Y. Wu, L. Xie, M. Wang, Q. Xiong, Y. Guo, Y. Liang, J. Li, R. Sheng, P. Deng, Y. Wang, R. Zheng, Y. Jiang, L. Ye, Q. Chen, X. Zhou, S. Lin, Q. Yuan, Mettl3-mediated m⁶A RNA methylation regulates the fate of bone marrow mesenchymal stem cells and osteoporosis, Nat. Commun. 9 (2018).

[21] G.M. Pagnotti, M. Styner, G. Uzer, V.S. Patel, L.E. Wright, K.K. Ness, T.A. Guise, J. Rubin, C.T. Rubin, Combating osteoporosis and obesity with exercise: leveraging cell mechanosensitivity, Nat. Rev. Endocrinol. 15 (6) (2019) 339–355.

[22] D. Tang, X. Chen, R. Kang, G. Kroemer, Ferroptosis: molecular mechanisms and health implications, Cell Res. 31 (2) (2021) 107–125.

[23] P. Liu, W. Wang, Z. Li, Y. Li, X. Yu, J. Tu, Z. Zhang, Ferroptosis: a new regulatory mechanism in osteoporosis, Oxid. Med. Cell. Longev. 2022 (2022).

[24] Y. Xia, H. Zhang, H. Wang, Q. Wang, P. Zhu, Y. Gu, H. Yang, D. Geng, Identification and validation of ferroptosis key genes in bone mesenchymal stromal cells of primary osteoporosis based on bioinformatics analysis, Front. Endocrinol. 13 (2022).

[25] L. Gao, W. Hua, L. Tian, X. Zhou, D. Wang, Y. Yang, G. Ni, Molecular mechanism of ferroptosis in orthopedic diseases, Cells 11 (19) (2022).

[26] S. Spriano, S. Yamaguchi, F. Baino, S. Ferraris, A critical review of multifunctional titanium surfaces: new frontiers for improving osseointegration and host response, avoiding bacteria contamination, Acta Biomater. 79 (2018) 1–22.

[27] D.D. Bosshardt, V. Chappuis, D. Buser, Osseointegration of titanium, titanium alloy and zirconia dental implants: current knowledge and open questions, 2000, Periodontol 73 (1) (2017) 22–40.

[28] M. Selim, L.D. Foster, C.S. Moy, G. Xi, M.D. Hill, L.B. Morgenstern, S.M. Greenberg, M.L. James, V. Singh, W.M. Clark, C. Norton, Y.Y. Palesch, S.D. Yeatts, D.E.F.I. i, Deferoxamine mesylate in patients with intracerebral haemorrhage (i-DEF): a multicentre, randomised, placebo-controlled, double-blind phase 2 trial, Lancet Neurol. 18 (5) (2019) 428–438.

[29] Z. Guo, J. Lin, K. Sun, J. Guo, X. Yao, G. Wang, L. Hou, J. Xu, J. Guo, F. Guo, Deferoxamine alleviates osteoarthritis by inhibiting chondrocyte ferroptosis and activating the Nrf2 pathway, Front. Pharmacol. 13 (2022).

[30] M.F. Hoes, N.G. Beverborg, J.D. Kijlstra, J. Kuipers, D. Swinkels, B.N.G. Giepmans, R.J. Rodenburg, D.J. van Veldhuisen, R.A. de Boer, P. van der Meer, Iron deficiency impairs contractility of human cardiomyocytes through decreased mitochondrial function, Eur. J. Heart Fail. 20 (5) (2018) 910–919.

[31] K.M. Monteiro Espindola, R.G. Ferreira, L.E. Mosquera Narvaez, A.C. Rocha Silva Rosario, A.H. Machado da Silva, A.G. Bispo Silva, A.P. Oliveira Vieira, M. C. Monteiro, Chemical and pharmacological aspects of caffeic acid and its activity in hepatocarcinoma, Front. Oncol. 9 (2019).

[32] S. Mirzaei, M.H. Gholami, A. Zabolian, H. Saleki, M.V. Farahani, S. Hamzehlou, F. B. Far, S.O. Sharifzadeh, S. Samarghandian, H. Khan, A.R. Aref, M. Ashrafizadeh, A. Zarrabi, G. Sethi, Caffeic acid and its derivatives as potential modulators of oncogenic molecular pathways: new hope in the fight against cancer, Pharmacol. Res. 171 (2021).

[33] S.S. Hallan, M. Sguizzato, P. Mariani, R. Cortesi, N. Huang, F. Simeliere, N. Marchetti, M. Drechsler, T. Ruzgas, E. Esposito, Design and characterization of ethosomes for transdermal delivery of caffeic acid, Pharmaceutics 12 (8) (2020).

[34] Y. He, Q. Chen, Y. Zhang, Y. Zhao, L. Chen, H₂O₂-Triggered rapid deposition of poly(caffeic acid) coatings: a mechanism-based entry to versatile and high-efficient molecular separation, Acs Appl. Mater. Inter. 12 (46) (2020) 52104–52115.

[35] D. Li, D. Wang, Y. Yang, P. Gao, W. Fan, X. Zhang, Y. Tang, W. Yang, K. Cai, Caffeic acid-deferoxamine self-polymerization coating on Ti implant promotes osteointegration by synergetic regulation of multi-pathways in ONFH mechanism, Adv. Funct. Mater. 33 (26) (2023).

[36] Y. Xie, S. Zhu, X. Song, X. Sun, Y. Fan, J. Liu, M. Zhong, H. Yuan, L. Zhang, T. R. Billiar, M.T. Lotze, H.J. Zeh III, R. Kang, G. Kroemer, D. Tang, The tumor suppressor p53 limits ferroptosis by blocking DPP4 activity, Cell Rep. 20 (7) (2017) 1692–1704.

[37] W.S. Yang, R. SriRamaratnam, M.E. Welsch, K. Shimada, R. Skouta, V. S. Viswanathan, J.H. Cheah, P.A. Clemons, A.F. Shamji, C.B. Clish, L.M. Brown, A. W. Girotti, V.W. Cornish, S.L. Schreiber, B.R. Stockwell, Regulation of ferroptotic cancer cell death by GPX4, Cell 156 (1–2) (2014) 317–331.

[38] Z.E. Stine, Z.E. Walton, B.J. Altman, A.L. Hsieh, C.V. Dang, MYC, metabolism, and cancer, Cancer Discov. 5 (10) (2015) 1024–1039.

[39] E.H. Kobayashi, T. Suzuki, R. Funayama, T. Nagashima, M. Hayashi, H. Sekine, N. Tanaka, T. Moriguchi, H. Motohashi, K. Nakayama, M. Yamamoto, Nrf2 suppresses macrophage inflammatory response by blocking proinflammatory cytokine transcription, Nat. Commun. 7 (2016).

[40] S.W. Ryter, Heme oxygenase-1: an anti-inflammatory effector in cardiovascular, lung, and related metabolic disorders, Antioxidants 11 (3) (2022).

[41] C.-Y. Huang, J.-S. Deng, W.-C. Huang, W.-P. Jiang, G.-J. Huang, Attenuation of lipopolysaccharide-induced acute lung injury by hispolon in mice, through regulating the TLR4/PI3K/Akt/mTOR and keap1/nrf2/HO-1 pathways, and suppressing oxidative stress-mediated ER stress-induced apoptosis and autophagy, Nutrients 12 (6) (2020).

[42] M. Chen, Y. Hu, Y. Hou, Y. Sun, M. Chen, M. Li, L. Tan, Z. Luo, K. Cai, Construction of a reactive oxygen species-responsive biomimetic multilayered titanium implant for in situ delivery of α-melanocyte-stimulating hormone to improve bone remolding in osteoporotic rats, Appl. Mater. Today 23 (2021).

[43] F.T. Shah, R. Chatterjee, M. Owusu-Asante, J.B. Porter, Adults with severe sickle cell anaemia and iron overload have a high incidence of osteopenia and osteoporosis, Blood 104 (2004) 1684.

[44] R. Bam, W. Ling, S. Khan, S.U. Venkateshaiah, X. Li, F. van Rhee, B. Nair, S. Usmani, B. Barlogie, J.D. Shaughnessy, J. Epstein, E.J. Anaissie, S. Yaccoby, Deregulated cellular iron metabolism factors mediate iron overload in myeloma cells and osteoclasts, and promote myeloma growth and bone disease, Blood 118 (2011) 3941.

[45] Y. Yang, Y. Lin, M. Wang, K. Yuan, Q. Wang, P. Mu, J. Du, Z. Yu, S. Yang, K. Huang, Y. Wang, H. Li, T. Tang, Targeting ferroptosis suppresses osteocyte glucolipotoxicity and alleviates diabetic osteoporosis, Bone Res. 10 (2022) 26.

[46] H. Bayir, S.J.J. Dixon, Y.Y.Y. Tyurina, J.A.A. Kellum, V.E.E. Kagan, Ferroptotic mechanisms and therapeutic targeting of iron metabolism and lipid peroxidation in the kidney, Nat. Rev. Nephrol. 19 (5) (2023) 315–336.

[47] P. Koppula, G. Lei, Y. Zhang, Y. Yan, C. Mao, L. Kondiparthi, J. Shi, X. Liu, A. Horbath, M. Das, W. Li, M.V. Poyurovsky, K. Olszewski, B. Gan, A targetable CoQ-FSP1 axis drives ferroptosis- and radiation-resistance in KEAP1 inactive lung cancers, Nat. Commun. 13 (1) (2022).

[48] X. Chen, J. Li, R. Kang, D.J. Klionsky, D. Tang, Ferroptosis: machinery and regulation, Autophagy 17 (9) (2021) 2054–2081.

[49] L. Jiang, N. Kon, T. Li, S.-J. Wang, T. Su, H. Hibshoosh, R. Baer, W. Gu, Ferroptosis as a p53-mediated activity during tumour suppression, Nature 520 (7545) (2015) 57.

[50] L. Wang, Y. Liu, T. Du, H. Yang, L. Lei, M. Guo, H.-F. Ding, J. Zhang, H. Wang, X. Chen, C. Yan, ATF3 promotes erastin-induced ferroptosis by suppressing system Xc, Cell Death Differ. 27 (2) (2020) 662–675.

[51] M.A. Badgley, D.M. Kremer, H.C. Maurer, K.E. DelGiorno, H.-J. Lee, V. Purohit, I. R. Sagalovskiy, A. Ma, J. Kapilian, C.E.M. Firl, A.R. Decker, S.A. Sastra, C. F. Palermo, L.R. Andrade, P. Sajjakulnukit, L. Zhang, Z.P. Tolstyka, T. Hirschhorn, C. Lamb, T. Liu, W. Gu, E.S. Seeley, E. Stone, G. Georgiou, U. Manor, A. Iuga, G. M. Wahl, B.R. Stockwell, C.A. Lyssiotis, K.P. Olive, Cysteine depletion induces pancreatic tumor ferroptosis in mice, Science 368 (6486) (2020) 85.

[52] P. Koppula, L. Zhuang, B. Gan, Cystine transporter SLC7A11/xCT in cancer: ferroptosis, nutrient dependency, and cancer therapy, Protein Cell 12 (8) (2021) 599–620.

[53] X. Shen, K. Fang, K.H.R. Yie, Z. Zhou, Y. Shen, S. Wu, Y. Zhu, Z. Deng, P. Ma, J. Ma, J. Liu, High proportion strontium-doped micro-arc oxidation coatings enhance early osseointegration of titanium in osteoporosis by anti-oxidative stress pathway, Bioact. Mater. 10 (2022) 405–419.

[54] A.S. Grillo, A.M. SantaMaria, M.D. Kafina, A.G. Cioffi, N.C. Huston, M. Han, Y. A. Seo, Y.Y. Yien, C. Nardone, A.V. Menon, J. Fan, D.C. Svoboda, J.B. Anderson, J. D. Hong, B.G. Nicolau, K. Subedi, A.A. Gewirth, M. Wessling-Resnick, J. Kim, B. H. Paw, M.D. Burke, Restored iron transport by a small molecule promotes absorption and hemoglobinization in animals, Science 356 (6338) (2017) 608–616.

[55] S.-R. Pasricha, J. Tye-Din, M.U. Muckenthaler, D.W. Swinkels, Iron deficiency, Lancet 397 (10270) (2021) 233–248.

[56] T. Korolnek, I. Hamza, Macrophages and iron trafficking at the birth and death of red cells, Blood 125 (19) (2015) 2893–2897.

[57] D.F. Edwards, C.J. Miller, A. Quintana-Martinez, C.S. Wright, M. Prideaux, G. J. Atkins, W.R. Thompson, E.L. Clinkenbeard, Differential iron requirements for osteoblast and adipocyte differentiation, JBMR Plus 5 (9) (2021) e10529.

[58] Q.W. Wang, B. Chen, M. Cao, J.F. Sun, H. Wu, P. Zhao, J. Xing, Y. Yang, X. Q. Zhang, M. Ji, N. Gu, Response of MAPK pathway to iron oxide nanoparticles in vitro treatment promotes osteogenic differentiation of hBMSCs, Biomaterials 86 (2016) 11–20.

[59] J. Jiang, J. He, S. Xiao, J. Shenyuan, T. Chen, D. Pei, Screening of superior anti-osteoporotic flavonoids from Epimedii Folium with dual effects of reversing iron overload and promoting osteogenesis, Biomed. Chromatogr. (2023) 5686.

[60] C.B. Billesbolle, C.M. Azumaya, R.C. Kretsch, A.S. Powers, S. Gonen, S. Schneider, T. Arvedson, R.O. Dror, Y. Cheng, A. Manglik, Structure of hepcidin-bound ferroportin reveals iron homeostatic mechanisms, Nature 586 (7831) (2020) 807.

[61] T. Ganz, Hepcidin and iron regulation, 10 years later, Blood 117 (17) (2011) 4425–4433.

[62] B.-D. Sui, C.-X. Zheng, M. Li, Y. Jin, C.-H. Hu, Epigenetic regulation of mesenchymal stem cell homeostasis, Trends Cell Biol. 30 (2019) 97.

[63] A. Rauch, A.K. Haakonsson, J.G.S. Madsen, M. Larsen, I. Forss, M.R. Madsen, E. L. Van Hauwaert, C. Wiwie, N.Z. Jespersen, M. Tencerova, R. Nielsen, B.D. Larsen, R. Röttger, J. Baumbach, C. Scheele, M. Kassem, S. Mandrup, Osteogenesis depends on commissioning of a network of stem cell transcription factors that act as repressors of adipogenesis, Nat. Genet. 51 (2019) 716.

[64] B.R. Stockwell, Ferroptosis turns 10: emerging mechanisms, physiological functions, and therapeutic applications, Cell 185 (14) (2022) 2401–2421.

[65] D. Gupta, S. Lessard, S. Dai, Y. Nakamura, A. Hicks, T.K. Harris, S. Krishnamoorthy, Genetic silencing of KEAP1 induces NRF2 mediated oxidative stress pathway in human erythroid cells, Blood 136 (2020).

[66] P. Ding, C. Gao, J. Zhou, J.L. Mei, G. Li, D.L. Liu, H. Li, P. Liao, M. Yao, B.Q. Wang, Y.F. Lu, X.Y. Peng, C.Y. Jiang, J.M. Yin, Y.G. Huang, M.H. Zheng, Y.S. Gao, C. Q. Zhang, J.J. Gao, Mitochondria from osteolineage cells regulate myeloid cell-mediated bone resorption, Nat. Commun. 15 (1) (2024) 5094.

[67] X.X. Ji, J.Q. Hong, W.N. Yang, M.J. Yao, J. Wang, G.Y. Jiang, Y.B. Wang, C.S. Li, J. Y. Lin, H.C. Mou, C.Z. Li, S.H. Li, Y.Z. Chen, M.M. Shi, W. Wang, F. Lu, H.B. Wu, X. Zhao, Y.Y. Qi, S.G. Yan, GSTP1-mediated S-glutathionylation of Pik3r1 is a redox hub that inhibits osteoclastogenesis through regulating autophagic flux, Redox Biol. 61 (2023) 102635.

[68] Y. Jeong, N.T. Hoang, A. Lovejoy, H. Stehr, A.M. Newman, A.J. Gentles, W. Kong, T. Diana, S. Martin, A. Chaudhuri, D. Heiser, L. Zhou, C. Say, J.N. Carter, S. M. Hiniker, B.W. Loo Jr., R.B. West, P. Beachy, A.A. Alizadeh, M. Diehn, Role of KEAP1/NRF2 and TP53 mutations in lung squamous cell carcinoma development and radiation resistance, Cancer Discov. 7 (1) (2017) 86–101.

[69] A. Cuadrado, A.I. Rojo, G. Wells, J.D. Hayes, S.P. Cousins, W.L. Rumsey, O. C. Attucks, S. Franklin, A.-L. Levonen, T.W. Kensler, A.T. Dinkova-Kostova, Therapeutic targeting of the NRF2 and KEAP 1 partnership in chronic diseases, Nat. Rev. Drug Discov. 18 (4) (2019) 295–317.

[70] M.A. Badgley, D.M. Kremer, H.C. Maurer, K.E. DelGiorno, H.J. Lee, V. Purohit, I. R. Sagalovskiy, A. Ma, J. Kapilian, C.E.M. Firl, A.R. Decker, S.A. Sastra, C. F. Palermo, L.R. Andrade, P. Sajjakulnukit, L. Zhang, Z.P. Tolstyka, T. Hirschhorn, C. Lamb, T. Liu, W. Gu, E.S. Seeley, E. Stone, G. Georgiou, U. Manor, A. Iuga, G. M. Wahl, B.R. Stockwell, C.A. Lyssiotis, K.P. Olive, Cysteine depletion induces pancreatic tumor ferroptosis in mice, Science 368 (6486) (2020) 85–89.